J. Fluid Mech. (2013), *vol.* 735, *pp.* 647–683.
doi:10.1017/jfm.2013.507

Sheet-like and plume-like thermal flow in a spherical convection experiment performed under microgravity

B. Futterer[1,2,†], A. Krebs[1], A.-C. Plesa[3], F. Zaussinger[1], R. Hollerbach[4], D. Breuer[3] and C. Egbers[1]

[1]Chair of Aerodynamics and Fluid Mechanics, Brandenburg University of Technology Cottbus, Siemens-Halske-Ring 14, 03046 Cottbus, Germany

[2]Institute of Fluid Dynamics and Thermodynamics, Otto von Guericke Universität Magdeburg, Universitätsplatz 18, 39106 Magdeburg, Germany

[3]Institute of Planetary Research, German Aerospace Center, Rutherfordstrasse 2, 12489 Berlin, Germany

[4]Institute of Geophysics, Earth and Planetary Magnetism Group, ETH Zürich, Sonneggstrasse 5, 8092 Zürich, Switzerland

(Received 8 February 2013; revised 21 August 2013; accepted 19 September 2013; first published online 29 October 2013)

We introduce, in spherical geometry, experiments on electro-hydrodynamic driven Rayleigh–Bénard convection that have been performed for both temperature-independent ('GeoFlow I') and temperature-dependent fluid viscosity properties ('GeoFlow II') with a measured viscosity contrast up to 1.5. To set up a self-gravitating force field, we use a high-voltage potential between the inner and outer boundaries and a dielectric insulating liquid; the experiments were performed under microgravity conditions on the International Space Station. We further run numerical simulations in three-dimensional spherical geometry to reproduce the results obtained in the 'GeoFlow' experiments. We use Wollaston prism shearing interferometry for flow visualization – an optical method producing fringe pattern images. The flow patterns differ between our two experiments. In 'GeoFlow I', we see a sheet-like thermal flow. In this case convection patterns have been successfully reproduced by three-dimensional numerical simulations using two different and independently developed codes. In contrast, in 'GeoFlow II', we obtain plume-like structures. Interestingly, numerical simulations do not yield this type of solution for the low viscosity contrast realized in the experiment. However, using a viscosity contrast of two orders of magnitude or higher, we can reproduce the patterns obtained in the 'GeoFlow II' experiment, from which we conclude that nonlinear effects shift the effective viscosity ratio.

Key words: Bénard convection, geophysical and geological flows, nonlinear dynamical systems

† Email address for correspondence: futterer@tu-cottbus.de

1. Introduction

Convection in spherical shells under the influence of a radial buoyancy force is of considerable interest in geophysical flows such as mantle convection (e.g. Schubert & Bercovici 2009). Laboratory experiments involving this configuration are complicated by the fact that gravity is then vertically downwards rather than radially inwards. One alternative is to conduct the experiment in microgravity, thereby switching off the vertically downward buoyancy force. Imposing a voltage difference between the inner and outer shells, and using the temperature dependence of the fluid's dielectric properties, can further create a radial force. The first such thermo-electro-hydrodynamic (TEHD) experiment was designed by Hart, Glatzmaier & Toomre (1986) using a hemispherical shell, and was accomplished on the space shuttle *Challenger* in May 1985.

A later experiment, called 'GeoFlow', not only involved a full shell instead of a hemisphere, but also was designed to be performed on the International Space Station (ISS), where considerably longer flight times are possible (Egbers *et al.* 2003). Two versions of 'GeoFlow' have now been accomplished: 'GeoFlow I', involving an essentially constant-viscosity fluid, was processed from August 2008 to January 2009 (Futterer *et al.* 2010); 'GeoFlow II', involving a fluid with pronounced temperature-dependent viscosity, was processed from March 2011 to May 2012 (Futterer *et al.* 2012). The purpose of this paper is to present an integrative comparison of the two experiments with one another, with accompanying numerical results, and with related results in the literature.

The arrangement of this paper is as follows. With the review in § 2, we present an extended literature study related to thermo-viscous Rayleigh–Bénard convection. There, we also address the differences between Cartesian and spherical geometries. Then, in § 3, we go through the physical basis for our TEHD experiment. The discussion of the list of properties involved in our experiment is the basis for linking the 'classical' spherical Rayleigh–Bénard system (driven by Archimedean buoyancy) with our TEHD driven Rayleigh–Bénard experiment. The final objective in this section is the calculation of the electric Rayleigh number from the experimental data and reordering it into domains available from the literature. The 'GeoFlow' experiment series uses a very specific flow visualization, the Wollaston schlieren interferometry or Wollaston prism shearing interferometry. The observed patterns of convection deliver fringe images, which requires additional knowledge on interpretation possibilities. This is demonstrated with a generic example in § 4. Then, in §§ 5 and 6 we discuss the experimentally observed flow regimes and corresponding numerical models for both experiment series 'GeoFlow I' and 'GeoFlow II'. Based on further numerical simulations, the deliberation of § 7 is on heat transfer properties related to different convective patterns. We summarize and give conclusions in § 8, involving a discussion on the nonlinear effects considered in our numerical models and an outlook for recently performed experiment series 'GeoFlow IIb'.

2. Thermally driven flow in liquids of temperature-dependent viscosity

In mantle dynamics, the basics of fluid flow movement and its interaction with tectonic plates are still the object of study. As extensively reviewed in Schubert & Bercovici (2009), research on those topics is focused on theoretical, numerical and experimental materials and methods, and moreover on the geophysical observations themselves. Especially, laboratory experiments have the character of 'exploring new physics and testing theories' (Davaille & Limare 2009). There, authors summarize the results from a huge series of tank experiments, which are designed to understand

Rayleigh–Bénard convection phenomena and its relations to overall mantle dynamics. They focus on the generation of plumes in highly viscous Newtonian and non-Newtonian liquids with a strong temperature dependence of the viscosity. Moreover, they describe their thermophysical and geometrical properties and present their interaction with the thermal boundaries. Finally, the authors relate their results to geophysical globally observed, convectively driven zones in the Earth's mantle.

Generally, in *simple* mantle dynamics (e.g. neglecting internal heating, and thermochemical or non-Newtonian convection), we consider the thermal driving of a Rayleigh–Bénard system filled with a highly viscous liquid by the Rayleigh number

$$Ra = \frac{\alpha g \Delta T d^3}{\nu_{ref}\kappa}, \tag{2.1}$$

using the following symbols: α, coefficient of volume expansion; g, acceleration due to gravity; $\Delta T = (T_{hot} - T_{ref})$, temperature difference between the geometrical boundaries, which are heated to T_{hot} and cooled at a reference value T_{ref}; d, characteristic length scale of the geometry (e.g. outer radius of a spherical shell system minus inner radius, $d = r_o - r_i$); ν_{ref}, reference kinematic viscosity; and κ, thermal diffusivity. From now on, we will consider that the reference index *ref* refers to the cool boundary of the system, where the various parameters are taken. With the Prandtl number

$$Pr = \frac{\nu_{ref}}{\kappa} \tag{2.2}$$

treated as infinite, $Pr \to \infty$, we ignore inertial effects. Typical values for the Earth's mantle are $\nu \to O(10^{16})$ and $\kappa \to O(10^{-7})$, and lead to this assumption (Schubert & Bercovici 2009). In this section we discuss results for thermally driven flow in fluids with temperature-dependent viscosity. This property is assessed with the viscosity ratio

$$\gamma = \frac{\nu_{ref}}{\nu_{(T_{ref}+\Delta T)}} = \frac{\nu_{cold}}{\nu_{hot}}, \tag{2.3}$$

which delivers the ratio between the reference viscosity at the cool boundary and the actual lowest possible viscosity at the hot boundary due to a specific temperature difference in the system. Further temperature-dependent properties, e.g. thermal expansion, seem to have a rather low impact on the dynamics (Ogawa 2008) compared to the viscosity effects. Complex double-diffusion convection models have been presented by, for example, Hansen & Yuen (1994). However, owing to our used homogeneous experimental fluid, chemical aspects are not regarded here.

During the past decades, various studies have addressed the topic of temperature-dependent viscosity mostly for Cartesian geometries (Booker 1976; Nataf & Richter 1982; Stengel, Oliver & Booker 1982; Richter, Nataf & Daly 1983; Morris & Canright 1984; Busse & Frick 1985; White 1988; Christensen & Harder 1991; Ogawa, Schubert & Zebib 1991; Hansen & Yuen 1993; Davaille & Jaupart 1994; Solomatov 1995; Tackley 1996; Kameyama & Ogawa 2000). While numerical simulations and laboratory experiments consider the Rayleigh–Bénard system in a rectangular box, naturally, the spherical shell convection is treated by means of numerical simulations only for constant viscosity (Baumgardner 1985; Bercovici, Schubert & Glatzmaier 1989*a*; Bercovici *et al.* 1989*b*; Bercovici, Schubert & Glatzmaier 1991, 1992; Schubert, Glatzmaier & Travis 1993) and for varying viscosity (Ratcliff, Schubert & Zebib 1996; Kellogg & King 1997; Ratcliff *et al.* 1997; Zhong *et al.* 2000; Yanagisawa & Yamagishi 2005; Stemmer, Harder & U Hansen 2006; Hernlund & Tackley 2008; Hüttig & Stemmer 2008*b*; Zhong *et al.* 2008; Hüttig & Breuer 2011).

To rearrange all the latter results in our context, we first refer to Solomatov (1995), who introduces scaling relations for three main viscosity contrasts in rectangular geometry, i.e. the mobile-lid, sluggish-lid and stagnant-lid convection. The mobile-lid domain is characterized by convection in isoviscous systems and systems with small viscosity contrast, where the surface layers are mobile and convection cells reach the outer/upper cold boundary of the spherical/Cartesian box domain. The sluggish-lid domain, also known as the transitional domain, is reached for larger viscosity contrasts, $\gamma \in (10^2, 10^4)$, resulting in a reduction of the velocity at the surface. In systems with viscosity contrasts $\gamma > 10^4$, convection develops below an immobile lid through which heat is transported only by conduction. In this regime stagnant-lid convection occurs. Ratcliff *et al.* (1997) and Hüttig & Breuer (2011) find a low-degree regime for bottom-heated and purely internally heated convection in a three-dimensional spherical shell, respectively. This regime has been found to lie between the mobile-lid and stagnant-lid domains and is characterized by long wavelengths. Low degrees for bottom-heated convection in a three-dimensional Cartesian box were also observed by Tackley (1993).

Moreover, Solomatov (1995) describes the mobile-lid domain behaving as a constant-viscosity domain with 'two thermal boundary layers of approximately equal thickness'. The limit between the mobile-lid and sluggish-lid domains not only is defined by the viscosity ratio itself, but also considers a different energetic balance of the cold and hot boundary layers. This is shown in figure 2 of Androvandi *et al.* (2011), where the authors collect all the relevant numerical and experimental contributions and describe the obtained convection pattern as a function of the top and bottom Rayleigh numbers in a three-dimensional Cartesian box geometry with

$$Ra_{hot} = \gamma\, Ra_{cold}, \tag{2.4}$$

when $Ra_{top} = Ra_{cold} = Ra$ (equation (2.1)). In figure 2 of Androvandi *et al.* (2011), the transition between mobile-lid and sluggish-lid domains is markedly analogous to the situation in Solomatov (1995) for a top Rayleigh number $Ra_{cold} = 10^6$ at $\gamma = 10^2$, whereas for $Ra_{cold} = 10^5$ the threshold is already at $\gamma = 10^1$. Thus, a sluggish-lid domain can be assessed by lower Rayleigh numbers and smaller viscosity contrasts; whereas for higher Ra, a higher viscosity ratio is needed to reach it.

Androvandi *et al.* (2011) collect experimental data from rigid boundary conditions in the same diagram together with numerical data from free-slip numerical simulations. In addition, the experiments investigate slightly different parameters in comparison to the numerical simulation. This might be related to the fact that frequently experiments run in a higher domain than numerical simulations achieve. However, experiments capture nonlinear effects and associated instabilities at most (Schubert & Olson 2009). It is also obvious that there are still huge regimes not fully assessed either with experiments or with numerical simulations. Nevertheless, the generic regimes for different fluid flow behaviours are visible in figure 2 of Androvandi *et al.* (2011). In the mobile-lid domain, if either the top or the bottom Ra is increased above a critical value, a transition from steady state to time-dependent convection can be observed. For supercritical Ra, plumes are the specific convective pattern not only for the nearly constant viscosity contrast, but also for the stagnant-lid domain. In the domains in between, we have a stabilization, i.e. transition from steady state to time-dependent behaviour occurs only at higher critical Ra. But the planform of convection becomes rather complex. Especially for intermediate viscosity ratio and high Ra, the authors capture the coexistence of several scales of convection, i.e. slabs and plumes.

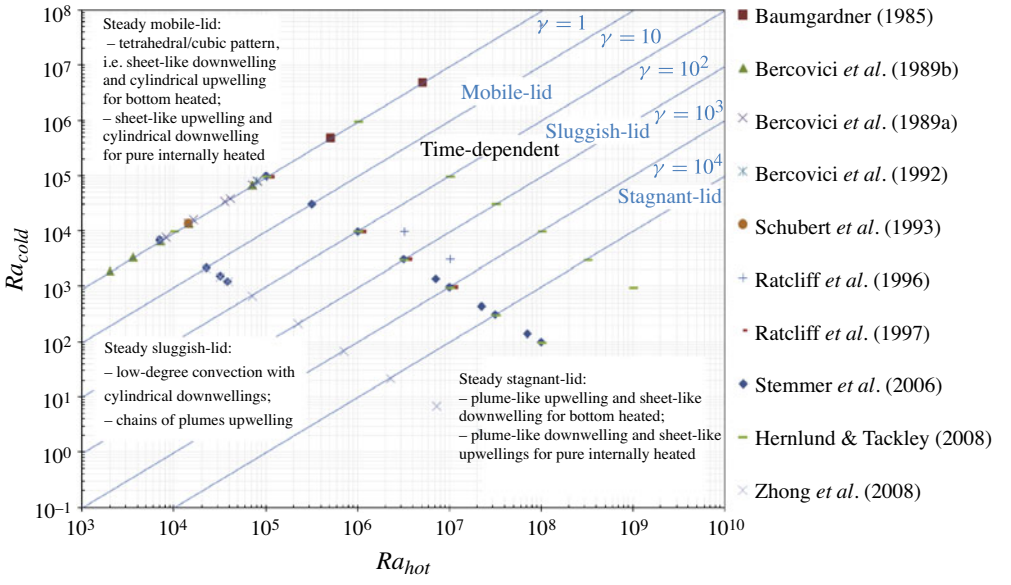

FIGURE 1. (Colour online) Spatio-temporal behaviour of incompressible, Newtonian Boussinesq convection in spherical shells as a function of cool outer Rayleigh and hot inner Rayleigh numbers related via the viscosity ratio by $Ra_{hot} = \gamma Ra_{cold}$ with $Ra_{cold} = Ra = (\alpha g \Delta T d^3)/(\nu_{ref}\kappa)$. The graphical illustration follows the idea from figure 2 in Androvandi *et al.* (2011), who introduced it for the Cartesian box. With the viscosity ratio γ we distinguish the mobile-lid ($\gamma < 10^2$), the sluggish-lid and stagnant-lid ($\gamma > 10^4$) domains. The description of the convective planform in the steady flow cases for all viscosity domains gives evidence on the influence of γ, i.e. isolated plumes are only induced via increasing the viscosity ratio. Considering internal heating reverses the direction of the thermally driven flow, e.g. from upwelling to downwelling, in comparison to bottom heated spherical shell convection. The transition to time dependence in the upper parameter domain is not described in the literature. In addition, it is not clearly discussed by means of periodicity or chaotic time series and therewith only assessed qualitatively.

For the spherical geometry, we present the different convecting regimes found in the literature in a similar way to Androvandi *et al.* (2011) for Cartesian geometry (figure 1). All the numerical simulations, which are of relevance here, are performed for a radius ratio of inner to outer spherical radius $\eta = r_i/r_o = 0.55$ and infinite Prandtl number $Pr \to \infty$ with free-slip boundary conditions assuming an incompressible Newtonian Boussinesq fluid. The authors vary the Rayleigh number up to $Ra_{1/2} = 10^7$ and consider the viscosity ratio up to $\gamma < 10^5$ via the Frank–Kamenetskii viscosity approximation, i.e. a linear approximation of the exponent in the Arrhenius law

$$\mu = a\, \mathrm{e}^{-\ln(\gamma)(T - T_{ref})}. \tag{2.5}$$

Commonly, they choose $Ra_{1/2}$, which references the viscosity at a non-dimensional temperature of 0.5 (note that the non-dimensional temperature is between 0 and 1 in the studied domain). Stemmer *et al.* (2006) give a general expression relating the different Rayleigh numbers $Ra_{1/2}$, Ra_{cold} and Ra_{hot} for our case to

$$Ra_{hot} = \gamma^{0.5}\, Ra_{1/2} = \gamma\, Ra_{cold}. \tag{2.6}$$

Especially for the control of experiments, it is more convenient to use either the inner or outer Rayleigh number at the hot or cool boundaries, respectively. In this paper our reference is always the lower Rayleigh number at the outer cool boundary.

By recalculating the specific Rayleigh numbers from (2.6), we collect the literature results from numerical experiments analogously to Androvandi *et al.* (2011), which results in our figure 1 for incompressible Newtonian Boussinesq fluids. The convective regimes are again divided into domains with low, transitional and high viscosity contrast, equivalent to mobile-, sluggish- and stagnant-lid domains. Note that it is also possible to use the term 'non-Boussinesq' related to such a strong temperature dependence of the kinematic viscosity of the fluid, which breaks the symmetry between the top and bottom boundary layers (Zhang, Childress & Libchaber 1997). To the best of our knowledge a scaling for the domains as presented in Solomatov (1995) is not available for three-dimensional spherical geometry apart from for purely internally heated convection (Hüttig & Breuer 2011), which is not under consideration here. Nevertheless, in figure 1 we observe for the constant and nearly constant viscosity domains the transition from steady to time-dependent flow states. However, the authors describe the time dependences for the planform of convection solely qualitatively. It is the planform of steady-state convection that differs clearly from the rectangular box. The spherical symmetry delivers the coexistence of two patterns, a tetrahedral and a cubic mode, which are both characterized by sheet-like downwellings and plume-like upwellings. The increase of the viscosity ratio induces the planform of cylindrical downwellings at the pole and a chain of plumes upwelling at the equator (Ratcliff *et al.* 1996). In the stagnant-lid domain, thermal up- and downwellings are in the form of plumes only. From the literature it is not possible to compare time-dependent patterns between the Cartesian and spherical geometries as they are not fully assessed. Only Ratcliff *et al.* (1997) present both systems concurrently. For the mobile-lid domain, they describe the upwelling to be sheet-like in the box, but plume-like in the sphere.

Besides the onset of convection for constant-viscosity fluids ($\gamma = 1$), which is $Ra_{hot} = Ra_{cold} = Ra = 712$ (Bercovici *et al.* 1989*a*; Ratcliff *et al.* 1996), detailed critical Rayleigh numbers for the transitions between different convective regimes are not available. That value for the onset is below the well-known value of $Ra = 1708$ in an infinite plane layer (Hébert *et al.* 2010). It is not possible to compare the two values directly, as for the spherical geometry the critical value depends on both the curvature $\delta = (r_o - r_i)/r_i$, which is related to the radius ratio by $\delta = 1/\eta - 1$, and the critical mode (Chandrasekhar 1981). If the radius ratio is increasing, we get into the limit of the plane layer reaching the value of $Ra = 1719$ (Zhang, Liao & Zhang 2002). If we have a lower η with higher δ, the critical Ra is decreasing (e.g. down to 712 for $\eta = 0.55$). Thus it is obvious that an increase of the curvature decreases the dimension of the hot boundary layer in comparison to the cold boundary layer. This imbalance might lead to a more unstable situation already at a smaller critical temperature difference, in addition to the thickness of the fluid layer increasing.

Generally, the viscosity contrast also has an influence on the critical Rayleigh number for the onset of convection. It decreases with increasing viscosity contrast if the reference is defined at the cold outer boundary. Ratcliff *et al.* (1996) present at $\eta = 0.55$, e.g. for $\gamma = 10^3$, $Ra_{1/2} = 2196$ (corresponding to $Ra_{cold} = 69$) as the critical Rayleigh number for self-sustaining convection with most unstable wavenumber $l_{crit} = 2$; and for $\gamma = 10^4$, $Ra_{1/2} = 3400$ with $l_{crit} = 4$ (corresponding to $Ra_{cold} = 34$). If, however, the reference Rayleigh number is defined at the lower boundary layer, we expect a competition between sphericity and temperature-dependent viscosity for the

onset of convection (Bercovici *et al.* 1989*a*, chapter 2, p. 77). This seems to be valid only if we consider the Rayleigh number at the hot boundary, which indeed increases analogously to (2.6) and in comparison to the values above.

With this summarized knowledge identifying also unresolved issues, we have to quantify the contribution of our experiment, i.e. the description of our parameter domains. Subsequently, the main objective is to calculate the specific Rayleigh number and viscosity ratio to reorder our data into a comparable regime set-up. This leads to the fact that our experiment will deliver the description of flow patterns in the lower-viscosity-contrast domain for several orders of the Rayleigh number. As already stated previously, a direct comparison may not be possible. The objective here is to compare the generic flow behaviour in specific parameter domains. For this we continue with the physical basics of TEHD driven flow in spherical shells.

3. Thermo-electro-hydrodynamic driven flow in spherical shells

We consider a fluid-filled spherical shell set-up, with the inner and outer boundaries maintained at different temperatures. The crucial challenge in spherical experiments is the set-up of a self-gravitating force field (Busse 2002), as in an Earth-based laboratory the gravitational field is aligned with a vertically directed unit vector $g\boldsymbol{e}_z$. To set up a radially directed buoyancy $g\boldsymbol{e}_r$, we apply an electric field $\boldsymbol{E}$ by a voltage potential V_0 with $\boldsymbol{E} = -\boldsymbol{\nabla} V_0$. Then we consider the electric body force

$$\boldsymbol{f}_E = \boldsymbol{f}_C + \boldsymbol{f}_{DEP} + \boldsymbol{f}_{ES}, \tag{3.1}$$

formed by the electrophoretic (Coulomb) force $\boldsymbol{f}_C$ and the dielectric force $\boldsymbol{f}_D$, which is composed of the dielectrophoretic force $\boldsymbol{f}_{DEP}$ and the electrostrictive force $\boldsymbol{f}_{ES}$. In detail we have from Landau, Lifshitz & Pitaevskii (1984) that

$$\boldsymbol{f}_E = q\boldsymbol{E} - \frac{1}{2}E^2\boldsymbol{\nabla}\varepsilon + \boldsymbol{\nabla}\left(\frac{1}{2}\rho E^2\frac{\partial\varepsilon}{\partial\rho}\right), \tag{3.2}$$

where $E = |\boldsymbol{E}|$. Applying direct current (d.c.), electric fields exert Coulomb forces; whereas in alternating current (a.c.) electric fields of high frequency $f \gg 1/\tau_E$ (with the charge relaxation time τ_E) the dielectrophoretic force $\boldsymbol{f}_{DEP}$ is dominant. In general, we can neglect the gradient force $\boldsymbol{f}_{ES}$ as it has no contribution to the flow field (Yoshikawa, Crumeyrolle & Mutabazi 2013). With the use of a high-frequency a.c. high-voltage potential V_0 between the spherical boundaries, we drop Coulomb effects in the electric body force, leading to

$$\boldsymbol{f}_E = \boldsymbol{f}_{DEP} = -\tfrac{1}{2}E^2\boldsymbol{\nabla}\varepsilon. \tag{3.3}$$

Finally, it is only this dielectrophoretic force that acts on a dielectric insulating liquid of temperature-dependent permittivity ε. To derive further relations we need information on (i) the electric field $\boldsymbol{E}$ and (ii) the temperature-dependent variation of the permittivity ε. Here, we just mention both relations; for more details, the interested reader is referred to Yavorskaya, Fomina & Balyaev (1984) and Hart *et al.* (1986) for application in the spherical shell and to Jones (1979) and more recently Yoshikawa *et al.* (2013) for the cylindrical annulus. For the calculation of the electric field, we treat the spherical shell as a spherical capacitor with

$$\boldsymbol{E}(\boldsymbol{r}) = \frac{r_i r_o}{r_o - r_i}\frac{1}{r^2}\boldsymbol{e}_r V_0. \tag{3.4}$$

For the variation of the permittivity we use

$$\varepsilon = \varepsilon_1[1 - \alpha_E(T - T_{ref})], \quad \varepsilon_1 = \varepsilon_0\varepsilon_r(T_{ref}), \tag{3.5}$$

with the relative permittivity ε_r and the vacuum permittivity ε_0. The coefficient of dielectric expansion α_E is related to the permittivity by $\partial\varepsilon/\partial T = -\varepsilon_0\varepsilon_r\alpha_E$. This corresponds to the coefficient of volume expansion as $\partial\rho/\partial T = -\rho_0\alpha$. This is in analogy to the 'classical' Boussinesq approximated Rayleigh–Bénard convection, which is mainly maintained by the temperature dependence of the density ρ with

$$\boldsymbol{f} = \alpha T\boldsymbol{g}, \quad \rho = \rho_0[1 - \alpha(T - T_{ref})], \quad \rho_0 = \rho(T_{ref}). \tag{3.6}$$

To summarize from Hart *et al.* (1986) and Yoshikawa *et al.* (2013), we have for the electric buoyancy force

$$\boldsymbol{f}_E = \alpha_E T\boldsymbol{g}_E, \quad \varepsilon = \varepsilon_1[1 - \alpha_E(T - T_{ref})], \quad \varepsilon_1 = \varepsilon_0\varepsilon_r(T_{ref}). \tag{3.7}$$

In this formulation we get an acceleration $\boldsymbol{g}_E$ defined by

$$\boldsymbol{g}_E = \frac{2\varepsilon_0\varepsilon_r}{\rho_{ref}}\left(\frac{r_i r_o}{r_o - r_i}\right)^2 V_0^2\frac{1}{r^5}\boldsymbol{e}_r. \tag{3.8}$$

It is obvious that this 'electric' gravity varies with the depth, i.e. at the inner boundary of the spherical shell we have a higher acceleration. Up to the outer boundary, the functional relation follows $1/r^5$, resulting in a lower gravity potential at that boundary.

The magnitude of the vector $\boldsymbol{g}_E$ reaches the order of up to 10^{-1} m s^{-2} at the outer spherical radius of our experiment (Futterer *et al.* 2010). This induces the need for microgravity conditions in order to get a pure radially directed electric buoyancy field not superimposed by the vertically directed Archimedean buoyancy forces (equation (3.6)). We consider, therefore, a TEHD convection in microgravity (equation (3.7)), which is driven by the temperature dependence of the electric permittivity ε. Next we have to discuss the 'difference' between the Archimedean buoyancy and electric buoyancy, mainly present in the radial dependence of the electric gravity and the coefficient of dielectric expansion. Thus, in the following, we present details on the dielectrophoretically induced self-gravitating force field in the equational set-up and later on further physical properties of our spherical TEHD Rayleigh–Bénard system.

3.1. *Different radial variations of radial gravity*

We consider the Boussinesq approximation to be valid for the description of the fluid motion, since the velocities appear to be small and the density fluctuations (and permittivity variations, respectively) are linear (Chandrasekhar 1981; Sugiyama *et al.* 2007; Futterer *et al.* 2012). The following relations are the basis for rescaling length r, time t, temperature T, the effective pressure P and the viscosity μ: $r = (r_o - r_i)r^* = dr^*$, $t = d^2/\kappa t^*$, $T - T_{ref} = \Delta T\,T^*$, $P = \kappa\nu/d^2P^*$ and $\mu = \mu_{ref}\mu^*$. Abandoning the *, the equations for mass and momentum conservation as well as the temperature become

$$\nabla\cdot\boldsymbol{u} = 0, \tag{3.9}$$

$$Pr^{-1}\left[\frac{\partial\boldsymbol{u}}{\partial t} + (\boldsymbol{u}\cdot\nabla)\boldsymbol{u}\right] = -\nabla P + \nabla\cdot[\mu(\nabla\boldsymbol{u} + (\nabla\boldsymbol{u})^{\mathrm{T}})] + Ra_E Tr^{-5}\boldsymbol{e}_r, \tag{3.10}$$

$$\frac{\partial T}{\partial t} + \boldsymbol{u}\cdot\nabla T = \nabla\cdot\nabla T, \tag{3.11}$$

with the inner radius r_i, the outer radius r_o and the unit vector in radial direction $\boldsymbol{e}_r$. Therewith, the thermal drive is now weighted by an electric Rayleigh number

$$Ra_E = \frac{\alpha_E \Delta T g_E d^3}{\nu_{ref}\kappa}\left(\frac{d}{r_o}\right)^{-5}. \tag{3.12}$$

With the depth-dependent gravity (3.8) we obtain different values at the hot and cool boundaries for the electric Rayleigh number ($\propto \boldsymbol{g}_E$), when a specific ΔT is regarded at a constant viscosity level. When we rewrite this equation by taking into account constants, geometrical aspects, temperature-dependent physical properties, reference physical properties and variational parameters, we obtain for the cold outer Rayleigh number

$$Ra_{E,cold} = \underbrace{2\varepsilon_0 V_0^2}_{const.}\ \underbrace{\frac{r_i^2 r_o^7}{d^4}\frac{1}{r_o^5}}_{geometry}\ \underbrace{\varepsilon_r(T_{cold})\alpha_E(T_{cold})}_{temp.\ dep.}\ \underbrace{\frac{1}{\mu_{cold}\kappa_{cold}}}_{references}\ \underbrace{\Delta T}_{variable}, \tag{3.13}$$

and for the hot inner Rayleigh number

$$Ra_{E,hot} = 2\varepsilon_0 V_0^2 \frac{r_i^2 r_o^7}{d^4}\frac{1}{r_i^5}\varepsilon_r(T_{hot})\alpha_E(T_{hot})\frac{1}{\mu_{hot}\kappa_{hot}}\Delta T. \tag{3.14}$$

Finally, we have

$$Ra_{E,hot} = \gamma\left(\frac{1}{\eta}\right)^5 \frac{\varepsilon_r(T_{hot})\alpha_E(T_{hot})}{\varepsilon_r(T_{cold})\alpha_E(T_{cold})} Ra_{E,cold}. \tag{3.15}$$

With $\eta = 0.5$ the initial difference between the cold and hot boundaries in their Ra_E amounts to a factor of 32. The range of the ratio resulting from relative permittivity ε_r and dielectric expansion coefficient α_E at the hot and cold boundaries depends on the experimental fluid and will be discussed later on. A subsequent question for the interpretation of our experimental data is whether these additional factors lead to an enhancement of the viscosity ratio for the fluid flow behaviour. But first, we have to choose $Ra_{E,cold}$ or $Ra_{E,hot}$ in our equation (3.10) consistently in order to avoid involving the electric Rayleigh number as a function and not as a parameter. From now on, we will always refer the electric Rayleigh number to the outer spherical radius. This is consistent with choosing the cool boundary as reference.

Now we assume that the TEHD driven convection has the property of a depth-dependent gravity and we seek comparable situations. In the mantles of planetary bodies, however, gravity is taken to be constant, whereas hydrodynamic convective modes in the Earth's liquid outer core are considered with a linear dependence (Busse 2002). In addition, for the Earth's atmosphere, the planet's gravitational potential acts with $1/r^2$, but here convective modes are mainly driven by rotational effects in differential heating at one surface. A classical spherical shell convection model, as regarded here especially with rigid boundary conditions and isothermally heated, is not considered here (Cullen 2007). Also, there is a clear tendency for setting up, for example, baroclinic situations in cylindrical geometry. The different radial dependences seem to become visible only in the planform of convection. Busse (1975) and Busse & Riahi (1982) regard the symmetry-breaking bifurcations in the spherical shell convection for the linear dependence of gravity. They already derive the generic nature of the branches with polyhedral modes. In Bercovici *et al.* (1989*b*) we find the confirmation of tetrahedral and cubic patterns as the dominating flow mode

for the constant-gravity case. In those flow structures the 'corners' of the patterns are the cylindrically formed upwellings. Feudel *et al.* (2011) show that the $1/r^5$ dependence induces axisymmetric and five-fold symmetries besides the cubic mode. The tetrahedral mode does not occur. In their case, the cubic mode is dominated by sheet-like upwellings near the hot boundary layer, besides the cylindrically formed upwellings. This is in contrast to the cubic mode of Bercovici *et al.* (1989*b*), for example, where no 'ridges' occur in between. This is a first hint that 'classical' plumes are a specific property of the constant-gravity case.

The objective to tend into a specific planform of convection seems to be a reduction of shear between upwellings and downwellings (Bercovici *et al.* 1989*a*). Owing to an increase of the rising or sinking velocity, the gravitational potential energy is released more efficiently. Bercovici *et al.* (1989*a*) claim that 'in three-dimensional convection with any geometry, a cylindrical upwelling or downwelling will necessarily be surrounded by a sheet-like return flow'. The differences between planar and spherical geometries, i.e. the asymmetry of up- and downwellings in the sphere, result from geometrical effects. Thus the specific radial dependence only results in different convection cell wavelengths. The whole scenario remains generic.

Therewith we can compare the classical and TEHD Rayleigh–Bénard system. For this we need to rescale our Rayleigh numbers due to the fact that (i) in mantle convection we have the buoyancy term $RaT\boldsymbol{e}_r$, and (ii) in 'GeoFlow' we have the buoyancy term $Ra_E Tr^{-5}\boldsymbol{e}_r$ in the momentum equation. The non-dimensional radii are $r_i^* = 1$ and $r_o^* = 2$, and the real dimensions of our experiments are $r_i = 13.5$ mm and $r_o = 27$ mm. To compare (i) and (ii), when running mantle convection tests (i.e. without r^{-5} in the buoyancy term), we take the reference at the top multiplied by the radial dependence, leading to $R_{E,cold}(r_o^*)^{-5}$. For example, if we have a Rayleigh number in 'GeoFlow' with $Ra_{E,cold} = 2 \times 10^4$, then a simulation run takes the Rayleigh number $Ra_{cold} = 2 \times 10^4 \times 2^{-5} = 2 \times 10^4/32 = 625$ to meet the corresponding mantle convection domain. With an additional test on the mean temperature profile and root mean squared velocity between the different buoyancy terms, we observe a clear difference in the magnitudes of the order of 10 in the velocity, if the factor $(r^*)^{-5} = 1/32$ is not considered. Finally, this leads to the Rayleigh domain for the 'GeoFlow' experiment series as depicted in figure 2. For our numerical simulation we perform both (i) the mantle set-up with constant gravity as well as (ii) the 'GeoFlow' set-up with variational gravity. For the mantle set-up, we simulate additional parameters in the neighbourhood of the experimental set-up.

We have already stated that the general symmetry of convective patterns does not depend on the functional form of the radial gravity. Now we can compare the critical Rayleigh numbers for the different cases. In a mantle model with $\eta = 0.55$ the onset of convection for the constant-viscosity case ($\gamma = 1$) occurs at $Ra_{hot} = Ra_{cold} = Ra = 712$, but in our own simulation, owing to the no-slip boundary conditions, we observe the onset with $Ra \in (2.1 \times 10^3, 2.2 \times 10^3]$. If we introduce a viscosity ratio, e.g. $\gamma = 32$, we get the onset with $Ra_{cold} \in (475, 500]$. Thus the viscosity contrast decreases the onset of convection.

For 'GeoFlow I' with $\eta = 0.5$ we observe it at $Ra_E|_{r_o} = 2491$ (Travnikov, Egbers & Hollerbach 2003; Feudel *et al.* 2011). Their Rayleigh number is related to the outer sphere and the equations are scaled besides others with the outer spherical radius r_o, which is in contrast to choosing the 'classical' gap width of the research cavity as characteristic length as introduced above for obtaining $Ra_E|_d = Ra_{E,cold}$. If we rescale their equations, we get $Ra_{E,cold} = 9964$ as critical onset. But to compare it with the constant-gravity case we have to divide this value by 32 and we

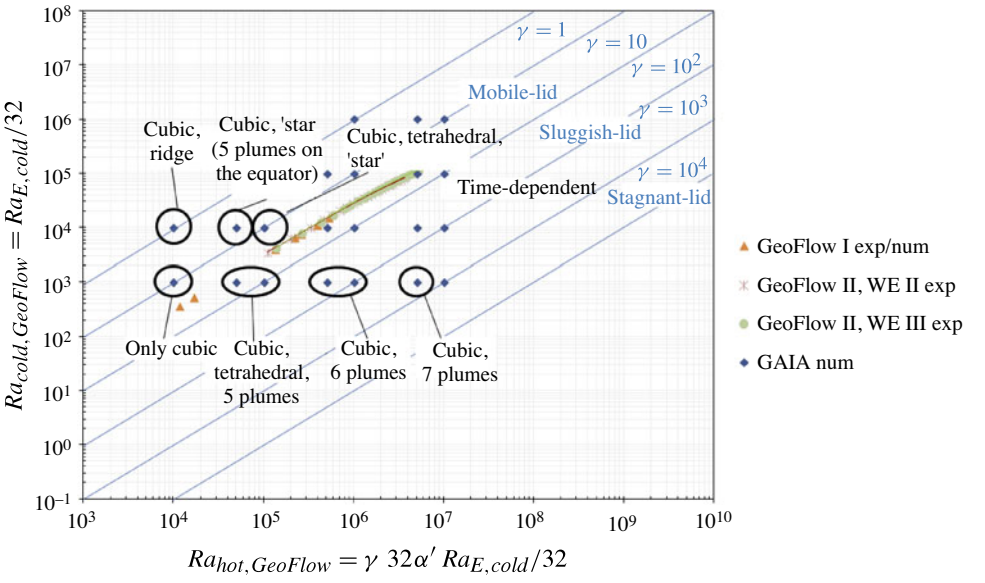

FIGURE 2. (Colour online) 'GeoFlow' experimental ('exp') and numerical ('num') parameter domains of incompressible, Newtonian TEHD Boussinesq convection in spherical shells as a function of cool outer Rayleigh and hot inner Rayleigh numbers related via the viscosity ratio by $Ra_{hot,GeoFlow} = \gamma 32\alpha' Ra_{cold,GeoFlow}$. For 'GeoFlow' we use the analogous electric Rayleigh number $Ra_{cold,GeoFlow} = Ra_{E,cold}/32 = [(\alpha_E g_E|_{r_o} \Delta T d^3)/(\nu_{ref}\kappa)(d/r_o)^{-5}]/32$ with the electric acceleration $g_E|_{r_o} = (2\varepsilon_0\varepsilon_r)/\rho_{ref}[r_i r_o/(r_o - r_i)]^2 V_0^2 r^{-5}$ related to the outer boundary $r = r_o$. For the development of the parameters related to TEHD effects, refer to § 3. 'GeoFlow II' is performed in two different working environments, 'WE II' and 'WE III', which differ in their reference viscosity. Specific 'GeoFlow' patterns of convection are described in §§ 5.1 and 6.1. From the illustration in figure 1 the classical convection regimes, i.e. stagnant-lid, sluggish-lid and mobile-lid, related to γ, are also included. In addition, the numerically simulated parameters $Ra_{hot} = \gamma Ra_{cold}$ for incompressible, Newtonian mantle Boussinesq convection in spherical shells are depicted ('GAIA num'). Again, increasing the viscosity ratio gives rise to plumes. The convective planform of stationary flow is precisely allocated. Unsteady time-dependent flow is characterized by plumes.

will have $Ra_{E,cold}/32 = 312$ for 'GeoFlow I'. It is worth mentioning that Travnikov *et al.* (2003) find the onset of isoviscous convection for decreasing radius ratio, too: $\eta = 0.4$, $Ra_E|_{r_o} = 1898$; $\eta = 0.3$, $Ra_E|_{r_o} = 1483$; $\eta = 0.2$, $Ra_E|_{r_o} = 1162$; and $\eta = 0.1$, $Ra_E|_{r_o} = 837$. This shows a decrease for the critical value if the curvature increases and corresponds to the general trend as reviewed in § 2 above. This is a further reason to treat the TEHD set-up as an analogue for a Rayleigh–Bénard system.

Up to now we have focused the discussion on the specific functional form of the gravity in the buoyancy term. But the physical properties of a real liquid are also the basis for the calculation of the Rayleigh number resulting in figure 2. We summarize the physical properties in tables 1 and 2, and their consideration in either non-dimensional parameters or equations in tables 3 and 4. Following the idea of (3.15) the two following subsections will discuss the temperature-dependent viscosity and the details of dielectric expansion. The objective is to clarify the magnitude of all three contributions.

Parameter		Unit	Value (at 25 °C)
Viscosity	ν_{ref}	$m^2\ s^{-1}$	5.00×10^{-6}
Thermal conductivity	λ	$W\ K^{-1}\ m^{-1}$	1.16×10^{-1}
Specific heat	c	$J\ kg^{-1}\ K^{-1}$	1.63×10^{3}
Density	ρ_{ref}	$kg\ m^{-3}$	9.20×10^{2}
Thermal diffusivity	$\kappa = \lambda/(\rho_{ref} c)$	$m^2\ s^{-1}$	7.74×10^{-8}
Thermal coefficient of volume expansion	α	1/K	1.08×10^{-3}
Relative permittivity	ε_r		2.7
Thermal coefficient of dielectric expansion (Yavorskaya *et al.* 1984; Hart *et al.* 1986)	$\alpha_E = \alpha(\varepsilon_r - 1)(\varepsilon_r + 2)/(3\varepsilon_r)$	1/K	1.07×10^{-3}

TABLE 1. Physical properties of the silicone oil M5, which is the experimental fluid of 'GeoFlow I'. We list the values of the parameters used in the experimental framework. As a well-defined liquid, all data are available from the data sheet (Bayer Leverkusen 2002).

Parameter		Value (at 20 °C)	Value (at 30 °C)
Viscosity	ν_{ref}	1.42×10^{-5}	9.73×10^{-6}
Thermal conductivity	λ	1.63×10^{-1}	1.58×10^{-1}
Specific heat	c	2.47×10^{3}	2.47×10^{3}
Density	ρ_{ref}	8.29×10^{2}	8.22×10^{2}
Thermal diffusivity	$\kappa = \lambda/(\rho_{ref} c)$	7.94×10^{-8}	7.76×10^{-8}
Thermal coefficient of volume expansion	α	9.45×10^{-4}	9.45×10^{-4}
Relative permittivity	ε_r	8.6	8.83
Thermal coefficient of dielectric expansion (Yavorskaya *et al.* 1984; Hart *et al.* 1986)	$\alpha_E = \alpha(\varepsilon_r - 1)(\varepsilon_r + 2)/(3\varepsilon_r)$	2.95×10^{-3}	2.46×10^{-3}
(new)	$-(1/\varepsilon_r)(\partial\varepsilon_r/\partial T)$	9.95×10^{-3}	9.71×10^{-3}

TABLE 2. Physical properties of the alkanol, 1-nonanol, which is the experimental fluid of 'GeoFlow II'. We list the values of the parameters for the two thermal working environments of the experiment, 'WE II' and 'WE III'. Alkanols are liquids whose physical properties are not always clearly quantified, especially in comparison to silicone oils. The cosmetics industry mainly employs 1-nonanol because of its lemon fragrance. We refer to data sheets from several companies (Merck 2003; FIZ Chemie 2010) and to the data collection from Lide (2008). The units are the same as in table 1 and are not listed due to limited space.

3.2. *Temperature-dependent viscosity*

In geodynamic models, the temperature-dependent dynamic viscosity μ, as part of the stress tensor, usually follows the Frank–Kamenetskii approximation of the Arrhenius law as in (2.5). If the liquid properties are temperature-independent, as for the silicone oil used in 'GeoFlow I', the relation is not of relevance and the viscosity is regarded as constant (Futterer *et al.* 2012). In (3.10) the viscous term becomes simpler with $\nabla^2 \boldsymbol{u}$. In 'GeoFlow II' we use an alkanol as experimental fluid with a pronounced variability of the viscosity with temperature leading to $\gamma \leqslant 1.5$. In Futterer *et al.*

Parameter	Thermal behaviour	Physical model
ν_{ref}	Linear with small slope, $\approx$ const. (measured at BTU)	Simple $\boldsymbol{\nabla u}$ in (3.10)
λ	Constant	Linear Fourier's law of thermal conduction in (3.11)
c	Estimated to be constant	—
ρ_{ref}	Linear (measured at BTU)	Boussinesq and Rayleigh number Ra and Ra_E
$\kappa = \lambda/(\rho_{ref} c)$	Calculated from λ, ρ, c	Reference Prandtl number Pr_{ref}
α	Constant	Boussinesq and Rayleigh number Ra and Ra_E, not of relevance in microgravity
ε_r	Constant	Analogue Boussinesq and Rayleigh number Ra_E
$\alpha_E = \alpha(\varepsilon_r - 1)(\varepsilon_r + 2)/(3\varepsilon_r)$	Calculated from ε_r	Analogue Boussinesq and Rayleigh number Ra_E

TABLE 3. 'GeoFlow I' experimental fluid, silicone oil M5. Overview of the general thermal behaviour and its consideration in a physical model, e.g. as approximation or equation. Silicone oils are liquids whose physical properties are clearly and accurately quantified (table 1). This is mainly due to their broad field of application. Therewith many data are available from the data sheet (Bayer Leverkusen 2002). In addition, we measured properties with significant experimental relevance (viscosity and density) at Brandenburg University of Technology (BTU).

(2012) we demonstrate the validity of (2.5) for our used experimental liquid. In Futterer *et al.* (2012) we present test cases of the Earth laboratory set-up, where the fluid-filled spherical shell is regarded as a heated inner sphere and cooled outer sphere corresponding to the fluid physics of natural convection in spherical enclosures (Futterer *et al.* 2007; Scurtu, Futterer & Egbers 2010).

In the Earth laboratory, the gravitational potential is no longer parallel to the heating and cooling surfaces. This results in a clear distinction from a Rayleigh–Bénard system by a base flow at infinitesimal small temperature difference induced by baroclinic vorticity (Dutton 1995; Bahloul, Mutabazi & Ambari 2000). Here the application of a high-voltage potential induces a slight enhancement of heat transfer via the created convective flow pattern. It acts as a possibility for flow control, but the variations of the permittivity are negligible due to the clear dominance of the density changes. This is the reason for conducting the experiment under microgravity conditions, where gravity and hence Archimedean buoyancy driven convection due to a unidirectional gravity field is absent. In Futterer *et al.* (2012) we only present experiments. In the recent work, we are able to reproduce those patterns by a numerical model following (3.9)–(3.11) and (2.5) For the preparatory studies we interpret the delivered patterns of convection to be induced by the temperature dependence of the viscosity.

3.3. *Thermal expansion in microgravity*

For the calculation of the Rayleigh number Ra_E in the microgravity experiments we have to include a temperature dependence of the thermal expansivity α_E if we

Parameter	Thermal behaviour	Physical model
ν_{ref}	Power law (measured at BTU/AP)	Arrhenius law
λ	Not available (implicit from Lide (2008))	Linear Fourier's law of thermal conduction in (3.11)
c	Not available (implicit from Lide (2008))	—
ρ_{ref}	Linear (measured at BTU)	Boussinesq and Rayleigh number Ra and Ra_E
$\kappa = \lambda/(\rho_{ref} c)$	Calculated from λ, ρ, c	Prandtl number Pr
α	Constant (data sheet from Merck)	Boussinesq and Rayleigh number Ra and Ra_E, not of relevance in microgravity
ε_r	Polynomial fit (data from FIZ)	Analogue Boussinesq and Rayleigh number Ra_E
$\alpha_E = \alpha(\varepsilon_r - 1)(\varepsilon_r + 2)/(3\varepsilon_r)$	Calculated from ε_r	Analogue Boussinesq and Rayleigh number Ra_E
$\alpha_E = -(1/\varepsilon_r)(\partial\varepsilon_r/\partial T)$	Calculated from ε_r	Analogue Boussinesq and Rayleigh number Ra_E

TABLE 4. 'GeoFlow II' experimental fluid alkanol, 1-nonanol. Overview of the general thermal behaviour and its consideration in a physical model, e.g. as approximation or equation. In addition to referring to data sheets from several companies (Merck 2003; FIZ Chemie 2010) and to the data collection from Lide (2008), we performed measurements of properties with significant experimental relevance (viscosity and density) at Brandenburg University of Technology (BTU) and at the company Anton Paar GmbH (AP).

use 1-nonanol instead of M5. It is a very specific property of silicone oils to be temperature-independent in all physical properties, and they are often only specified by their different viscosities. The decision to use 1-nonanol in the same experimental set-up is promoted through the overall comparable technical behaviour and the variability of the viscosity. In addition, we take into account the temperature dependence of the permittivity in (3.7), this being focused upon in the microgravity environment as a substitute for density in (3.6).

Up to now the calculation of the TEHD expansion coefficient α_E has been derived via the relation from Yavorskaya *et al.* (1984) and Hart *et al.* (1986):

$$\alpha_E = \alpha \frac{(\varepsilon_r - 1)(\varepsilon_r + 2)}{3\varepsilon_r}. \tag{3.16}$$

Behind this, we assume, is the following statement: 'equivalent to that usually made for a Boussinesq liquid, that ε is assumed constant except where multiplied by the electrostatic gravity' (Hart *et al.* 1986, p. 523). Regarding the liquid properties of M5 (Bayer Leverkusen 2002), this assumption is absolutely valid. But for 1-nonanol a measurement curve for ε_r with variation of the temperature T (FIZ Chemie 2010) and its polynomial fit with $\varepsilon_r = f(T) = 0.0005T^2 - 0.1063T + 10.595$ requires further consideration here. With

$$\alpha_E = -\frac{1}{\varepsilon_r}\frac{\partial \varepsilon_r}{\partial T} = -10^{-6}T^2 + 5 \times 10^{-5}T + 0.0096, \tag{3.17}$$

we get for the specific reference temperature and temperature difference a factor that is approximately 10 times higher than with (3.16) and therewith resulting in a different Ra_E. But in the working environment of the experiments it remains a linear behaviour like the natural volume expansion coefficient and will not need a further equation. Using the information from the physical properties, the contribution

$$\alpha' = \frac{\varepsilon_r(T_{hot})\alpha_E(T_{hot})}{\varepsilon_r(T_{cold})\alpha_E(T_{cold})} \geqslant 0.87 \tag{3.18}$$

remains of the order of one.

In order to investigate nonlinear effects in addition to focusing on the temperature dependence, we test an extended standard Boussinesq approximation. The main idea is based on an extension of the electric buoyancy force $\boldsymbol{f}_E$ in (3.7) by a quadratic term, $\beta_E(T - T_{ref})^2$. This results in an altered Rayleigh number $Ra_{E2} := Ra_E[1 - (\beta_E/\alpha_E)(T - T_{ref})]$. By choosing β_E sufficiently small, hence focusing mainly on the linear temperature dependence, the influence of the second-order term vanishes. Owing to the fact that measurements of the working fluid's density indicate only a minor quadratic dependence on temperature, the numerical test is performed with small values of Ra_{E2}. The overall solution does not change under the given assumptions. Hence, the first-order Boussinesq approximation is an adequate and valid truncation, reproducing the correct fluid flows in the depicted parameter space. Here, we refer to a comprehensive review on nonlinear properties of convection given by Busse (1978).

3.4. *Effects from Prandtl number, radius ratio and boundary conditions*

Besides the impact of the radial dependence in the buoyancy term and the calculation of a suitable Rayleigh number, the left side of (3.10) requires a short comment on the influence of the Prandtl number $Pr = \nu_{ref}/\kappa$. Indeed, in our experiments, we have a finite Prandtl number with $Pr_{GeoFlow\,I} \approx 65$ and $Pr_{GeoFlow\,II} = 125$ and 200. When comparing the solutions with finite and infinite Pr, a benchmark with our two available codes (Hollerbach 2000) and GAIA (Hüttig & Stemmer 2008*a*), adapted for the TEHD model, delivers differences in the Nusselt number only of the order of 10^{-2} and reproduces the planform of convection with a very good agreement (Futterer *et al.* 2009). Additionally, both codes are well established for spherical shell convection issues in geo- and astrophysical research; therefore we refer the reader to the literature. In this present work the goal is to apply the codes to our experimental set-up. As a conclusion from the simulations, the Prandtl number might be disregarded in the numerical simulation and is considered also to have a negligible impact in the experiment.

Further tests have been done to address the differences between our experiment and state-of-the-art mantle convection models due to the radius ratio η, which is 0.5 for 'GeoFlow' and 0.55 for the mantle. If we use 0.5 instead of 0.55 we observe a minimal influence on the velocity and temperature (both velocity and temperature are negligibly smaller than in the 0.55 case).

A final remark has to be made on the boundary conditions. Naturally our closed experiment has no-slip conditions, but the mantle studies perform numerical simulations with free-slip conditions. Our tests deliver lower velocities for no-slip conditions, i.e. the convection is less vigorous than in free-slip cases, and higher temperatures, but no additional convection patterns with new symmetry classes were obtained.

3.5. *Summary*

From the previous discussion on the depth-dependent gravity, the temperature-dependent viscosity ratio and the thermal expansion in microgravity, we can conclude for (3.15) that

$$Ra_{E,hot}|_{max} = 1.5 \times 32 \times 0.9 \times Ra_{E,cold}. \tag{3.19}$$

Considering the factors, we assume an accuracy of one digit after the decimal point as relevant impact for this equation. For the temperature-independent silicone oil in 'GeoFlow I' we derive $\gamma \in (1.0, 1.1)$ and $\alpha' = 1.0$, whereas with the use of the temperature-dependent alkanol in 'GeoFlow II' we have $\gamma \in (1.0, 1.5)$ and $\alpha' \in (0.9, 1.0)$. The influence of the depth-dependent gravity remains constant with $(1/\eta)^5 = 32$ in both experiments. Considering also the scaling down on both sides of this equation with 1/32, we revisit figure 2. This demonstrates the enhancement of the viscosity contrast by the dominating factor of 32, in which γ is initially assessed only via the liquid itself to be in the range between 1 and 2. The contribution from dielectric thermal expansion seems even to damp down slightly the small viscosity contrast. Finally we conclude at this stage that both experiments mainly differ in their Rayleigh number regime 'distributed' along an enhanced viscosity ratio of 32. Referring figure 2 to figure 1, we expect to be able to describe the dynamics of the nearly constant-viscosity domain with 'GeoFlow I'. With 'GeoFlow II' we might capture domains of transitional dynamics of the higher viscosity contrast domains.

In figure 3 we depict the variation of the cold Rayleigh number related to the liquid-related viscosity contrast. This image does not take into account the enhancement via the factor 32. But this is necessary for the experimental protocol, as the pumping of the liquid in the cooling circuit is related to its viscosity, too. It is assumed that this is the most important parameter, which is varied according to experimental protocol via (i) choosing a reference environment to be either $T_{ref} = 20\,^{\circ}\mathrm{C}$ or $30\,^{\circ}\mathrm{C}$ for the viscosity variation up to $\gamma \approx 1.5$ and (ii) increasing the temperature difference between the inner and outer spherical shell boundaries up to $\Delta T = 10$ K. The high-voltage potential V_0 is set at the beginning of the experiment as this produces the electro-hydrodynamic buoyancy in the microgravity environment. For 'GeoFlow I' it is $V_0 = 10$ kV; in 'GeoFlow II' a lower value with $V_0 = 6.5$ kV is sufficient due to the higher relative permittivity of 1-nonanol.

4. A generic example for flow visualization

In the 'GeoFlow' experiment series, we use an optical method for flow visualization (Merzkirch 1987) as delivered by the Optical Diagnostics Module (ODM) of the Fluid Science Laboratory, more precisely the Wollaston prism shearing interferometer (WSI) introduced by Dubois *et al.* (1999). The method detects variations in the fluid refractive index, which reflects changes in the density (and the permittivity) of the fluid. Refractive index gradients are visualized either by a deflection of light or by phase shift disturbances, which are measured by such interferometers (Merzkirch 1987). At the least, the WSI yields images with *fringe* patterns of convection. Then the distances between the fringe lines measured in the resolving direction correspond with the magnitude of the directional derivative of the temperature field. The resolution is related to the polarization angle ω of the Wollaston prism, the main optical component of the WSI set-up. The following generic example explains how the fringe pattern can be used to discriminate between sheet-like and plume-like flow upwellings.

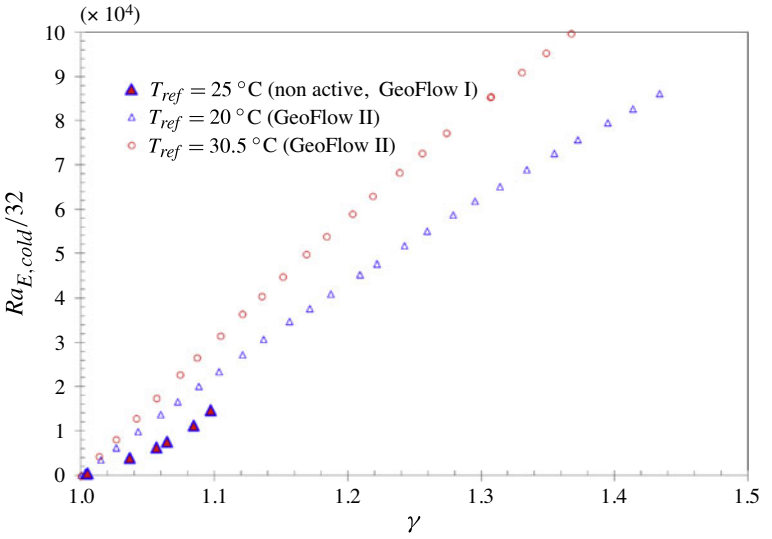

FIGURE 3. (Colour online) Rayleigh number as a function of the viscosity ratio in 'GeoFlow' experiments at spherical shells of radius ratio $\eta = 0.5$ filled either with silicone oil (▲) or alkanol (△, ◯). The experimental protocol is as follows: set-up of desired voltage V_0; reference image recording ($V_0 =$ desired value, $\Delta T = 0$, $n = 0.008$ Hz); loop on temperature difference ΔT with different start values and fixed increments including set-up of desired ΔT; wait time corresponding for thermal time scale $\tau = d^2/\kappa_{ref}$ for stabilization; scientific pictures acquisition, to be repeated at next ΔT (Mazzoni 2011). During 'GeoFlow I' the cooling loop kept its temperature in the vicinity of the ISS FSL temperature of 25 °C. The heat loss of the system to the environment was assumed to be negligible. During 'GeoFlow II' the cooling loop was controlled actively at either 20 °C or 30 °C, in order to control the reference viscosity. In this illustration the 'GeoFlow I' and 'II' domains differ clearly. The viscosity contrast here is related only to the behaviour of the real liquid.

We consider a fluid flow event given in the Cartesian box $[-1, 1]^2 \times d'$, where $d' > 0$ is small in comparison with the extension of the horizontal square $[-1, 1]^2$. As the measurement technique is an integrative method along the measurement section, we assume the temperature distribution of the fluid to be sufficiently well represented by the mean temperature taken in the approximate path of the laser light beam, i.e. the vertical direction (z goes from 0 to d'):

$$H(\boldsymbol{x}) := \frac{1}{d'} \int_0^{d'} T(\boldsymbol{x}, z)\, \mathrm{d}z. \tag{4.1}$$

Therefore, it remains to consider the two-dimensional temperature distribution $H(\boldsymbol{x})$ on the $[-1, 1]$ square. We generate comparable temperature sheet-like and plume-like flow upwellings using the following one-dimensional temperature flow profile function $h : \mathbb{R}_{\geqslant 0} \to \mathbb{R}_{\geqslant 0}$ given by

$$h(u) := \frac{1}{4} \begin{cases} (2-u)^3 - 4(1-u)^3 & \text{for } u \leqslant 1, \\ (2-u)^3 & \text{for } 1 < u \leqslant 2, \\ 0 & \text{for } 2 < u. \end{cases} \tag{4.2}$$

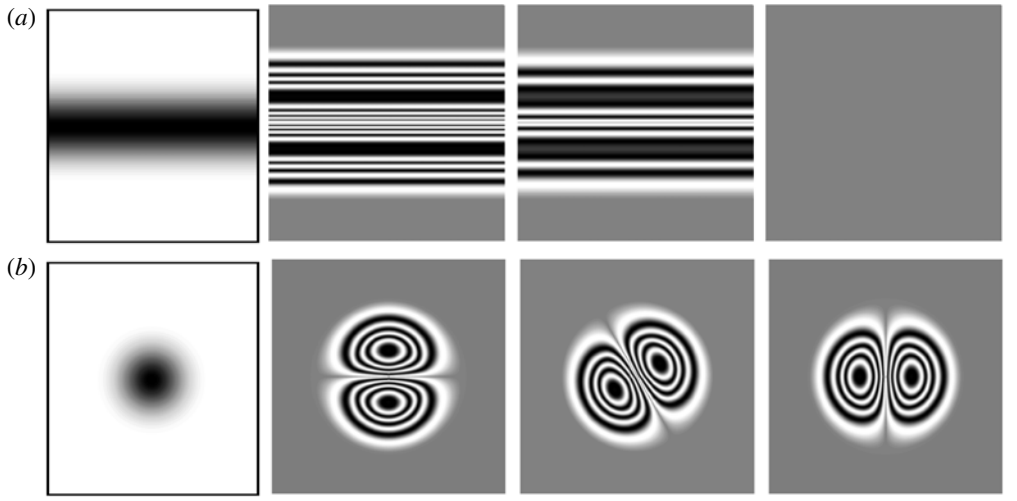

FIGURE 4. Flow visualization by means of Wollaston prism shearing interferometry: generic example. Column 1: contour plots of the sheet-like H_S (top) and the plume-like H_P temperature distributions (bottom). Columns 2–4: related fringe patterns of convection in interferograms for three directions of polarization of the Wollaston prism, $\omega = 90°$ (vertical), 30° and 0° (horizontal).

We obtain the plume-like temperature field H_P by rotating this cubic spline around the vertical axis:

$$H_P(\boldsymbol{x}) := h(\tfrac{1}{3}|\boldsymbol{x}|). \tag{4.3}$$

The sheet-like temperature field H_S is yielded by shifting the profile orthogonal to its plane:

$$H_S(\boldsymbol{x}) := h(\tfrac{1}{3}|x_2|). \tag{4.4}$$

The two temperature fields are presented by the contour plots in the left column of figure 4.

Assuming that the distances of the interferometry curves depend linearly on the magnitude of the directional derivative of the temperature field, we compute the corresponding fringe patterns for three directions of the polarization. The second column shows the patterns for the vertical direction ($\omega = 90°$), the last column for the horizontal direction ($\omega = 0°$), and the third column for the direction with an angle of $\omega = 30°$ to the horizontal axis. We use $\sin \Lambda\, |\partial H/\partial \boldsymbol{n}|$ as fringe generator, with a laser wavelength of $\Lambda = 532$ nm.

Using the generic example we obtain the following characterization of the sheet- and plume-like temperature upwellings:

(a) The interferogram of a sheet-like upwelling consists of parallel lines. The number of black lines reaches a maximum when the direction of polarization is orthogonal to the temperature isolines and decreases when the angle between the direction of polarization and the 'sheet' direction tends to zero. Therefrom we cannot detect sheet-like upwellings, which run parallel to the direction of polarization (figure 4, row 1, column 4).

(b) The interferogram of a plume-like upwelling is characterized by a double ring structure. The symmetry axis in between the ring pair is orthogonal to the direction of polarization. With it we possess a rule of thumb to determine the direction of polarization on unclassified interferograms of plume-like upwellings.

5. Sheet-like upwellings in a self-gravitating spherical shell experiment

5.1. *Experimental observation*

To navigate on the sphere, we use a spherical coordinate system with radial r, azimuthal φ and meridional θ directions. The rotation axis in the centre of the sphere corresponds to an angle $\theta = 0°$. The optical axis of the FSL camera, used to obtain the interferograms of the 'GeoFlow' experiment, intersects the spherical centre with an angle of $\theta = 30°$. The angle of beam spread from the WSI covers 88° on the sphere. Therewith the images taken from the sphere range from $\theta = -14°$ beyond the north pole down to $\theta = 74°$ near the south pole. In this way, we can map the position of an interferogram pixel onto the sphere.

As we want to collect as much image information as possible of the sphere's surface, we rotate the sphere with the slowest possible rotation frequency of $n = 0.008$ Hz and take a photo every $\varphi_i = 60°$ of the rotation, i.e. with $i = 6$ one photo every $[1/(0.008\ \mathrm{s}^{-1})]/6 = 20.83$ s. Neglecting the overlapping regions of these images, we use one photo to compute a sphere segment interferogram that sweeps the azimuthal from $-30°$ up to 30° of the meridian containing the optical axis. The north–south extension of this segment goes from the north pole down to the parallel $\theta = 74°$ near the equator. The montage of six interferograms is presented in figure 5. The six positions of the optical axes are marked by black crosses. The white meridians are the boundaries between the separate interferograms. The direction of interpolation is given by the grey parallel lines in one separate interferogram. The white rings show the parallels with $\theta = 15$, 30, 45 and 60° counted from the north pole. The equator is marked by the bold black line.

The lowest experimentally available $Ra_{E,cold}/32 = 5.18 \times 10^2$ at $\Delta T = 0.3$ K delivers images identical to the reference images, which are collected before setting up the parameters at $\Delta T = 0$ (figure 5*d*). At the next Rayleigh number $Ra_{E,cold}/32 = 6.44 \times 10^3$ we observe a very clear singular pattern of fine lines (figure 5*c*). At $Ra_{E,cold}/32 = 1.11 \times 10^4$ the gradients increase with an increase of line density and experience turning into hooks (figure 5*b*). At the experimentally observable limit of $Ra_{E,cold}/32 = 1.46 \times 10^4$ the patterns form sets of broader thermal upwellings in addition to some finer remaining fringe lines (figure 5*a*). All fringe patterns of convection correlate with sheet-like upwellings.

Considering the onset of convection in the stability analysis at $Ra_{E,cold}/32 = 3.12 \times 10^2$ in comparison to the assessed Rayleigh domain, we would expect to be always above the onset of convection. There are two possible reasons for observing no fringes at $Ra_{E,cold}/32 = 5.18 \times 10^2$. On the one hand, there might be a shift between stability analysis and experimental measurement. On the other hand, interferometry requires a critical temperature difference, which is necessary to produce fringes. For the lowest parameter domain $Ra_{E,cold}/32 \in (2 \times 10^2, 6 \times 10^3)$ we have no more data available due to technical problems on orbit. Thus we are not able to detect the onset of convection in the experiment precisely related to the specific critical temperature difference.

All samples are snapshots of time-dependent flows. For the real experimental velocity we can estimate the time frame of one turn in order to get back to the

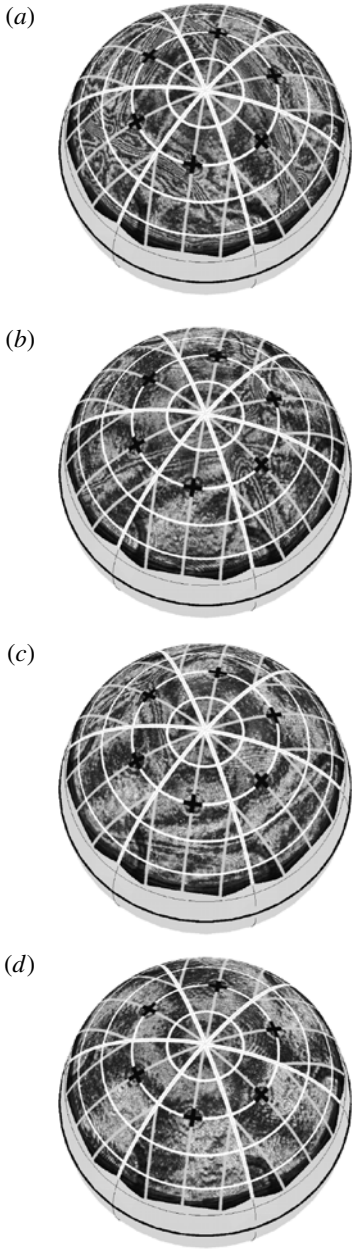

FIGURE 5. The TEHD spherical shell convection experiment 'GeoFlow I' with temperature-independent physical properties of the liquid (silicone oil with $Pr = 65$). Sheet-like upwelling fringe patterns of convection for variation of the Rayleigh number $Ra_{E,cold}/32$ at (*a*) 1.46×10^4, (*b*) 1.11×10^4 and (*c*) 6.44×10^3. Flow without specific pattern or even below onset of convection at (*d*) 5.19×10^2. Increase of thermal driving enhances sheet-like convective planform and increases the global velocity, which is not of high amplitude.

same image position again, which is $t = 1/(0.008\ \text{Hz}) = 125$ s. During that time of approximately 2 min, the patterns at a specific position on the image move only slightly in general, but not at the same rate over the whole image itself. To collect the

spatial change of the whole pattern in between two images, an automated procedure of image processing is a requirement, which is not available for those complex image data. Neither commercial software nor self-developed tools have fulfilled our objectives. That makes it impossible to assume one single velocity and requires an extended review of available methods. However, this is not the focus of this work. We conclude here that we observe sheet-like upwellings with long-term time-dependent behaviour.

5.2. *Numerical simulation*

In § 3 we present the governing equations of the TEHD driven Rayleigh–Bénard convection, which govern the fluid dynamics of the 'GeoFlow' experiment in particular. This theory is used to compute the temperature distribution of the fluid in the spherical shell. We apply the numerical code from Hollerbach (2000), i.e. a spectral method for the three-dimensional numerical simulation of the equations (3.9)–(3.11). We refer the reader to Hollerbach (2000) for a detailed description of the spectral solution in the magnetohydrodynamic framework. The no-slip boundary conditions on the velocity field and the fixed temperature values at the inner and outer shell close our set of equations. In Travnikov *et al.* (2003), Futterer *et al.* (2010) and Feudel *et al.* (2011), we have extensively applied the code to ideal isoviscous fluids with $\gamma = 1$. We summarize the most important results of Futterer *et al.* (2010) with a focus on the agreement with the experimental data, and those of Feudel *et al.* (2011) with the bifurcation scenario resulting from path following analysis in numerical simulations.

In the numerical simulation we observe the onset of convection at $Ra_{E,cold}/32 = 3.12 \times 10^2$. On increasing the Rayleigh number up to $Ra_{E,cold}/32 = 3.13 \times 10^3$, the results depict a steady-state convection with the coexistence of cubic, axisymmetric and five-fold symmetry classes. The transition to time-dependent states occurs suddenly; the time evolution delivers a very slow motion comparable to those observed in the experimental data. The available experimental data agree with the numerical data in the time-dependent domain. For this domain we choose to present data from the non-stationary regime and the agreement with experimental data in figure 6.

The time-dependent pattern of the TEHD driven analogous Rayleigh–Bénard Boussinesq convection combines the properties of all steady-state patterns from the lower Rayleigh domain. In the chosen snapshot in figure 6 we observe the cubic pattern produced by sheet-like upwellings in the radial velocity field illustration. This is also present in the temperature field data, when it is visualized on a spherical surface. To represent the details of the thermal upwellings, we plot also the temperature field in a cut and highlight an arbitrarily chosen isosurface of the temperature. There are no distinct plumes, but broadly merged thermal flow, i.e. sheet-like upwellings.

In order to compare the numerical simulations with the experiment, we compute the fringe patterns for a given temperature distribution $T(\varphi, \theta, r)$ with the approach of § 4. Again, we compute the mean of the temperature distribution in the approximate direction of light, i.e. in the radial direction from the inner to outer radius of the experiment geometry. Thus, we reduce the complexity of the temperature distribution to the following distribution to a surface of a sphere:

$$H(\varphi, \theta) := \frac{1}{r_o - r_i} \int_{r_i}^{r_o} T(\varphi, \theta, r)\, \mathrm{d}r. \tag{5.1}$$

Let us consider the experimental interferogram given in figure 6. The 60° meridians are visible via their intersection at the north pole. Again, the black cross marks the

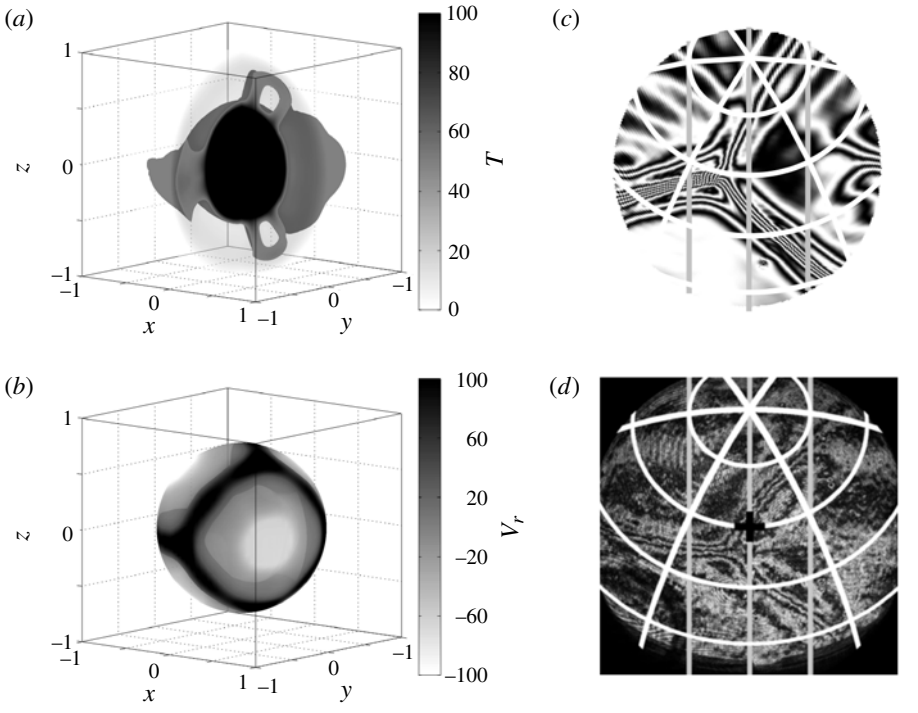

FIGURE 6. Numerical simulation of 'GeoFlow I' Boussinesq TEHD model with constant viscosity: (*a*) snapshot of sample at $Ra_{E,cold}/32 = 6.25 \times 10^3$ with non-dimensional temperature field distributed in the sphere and highlighted isosurface of $T = 0.5$; (*b*) radial velocity component in a mid-spherical surface $r = 0.5$. Fringe patterns of convection with sheet-like thermal upwelling (*c*) from numerical simulation of 'GeoFlow I' Boussinesq TEHD model with constant viscosity at $Ra_{E,cold}/32 = 6.25 \times 10^3$, and (*d*) observed in a raw image in the experiments at $Ra_{E,cold}/32 = 6.44 \times 10^3$.

centre of the circle-shaped image; it is equivalently the intersection of the sphere with the optical axis. The grey parallels depict the direction of polarization of the interferogram. We compute the gradient $\boldsymbol{\nabla}_{\varphi,\theta} H$ from the numerical data by taking the central differences and obtain $\partial H(\varphi, \theta)/\partial \boldsymbol{n}$ via the multidimensional chain rule of differentiation applied to the rotational transformations. Again, we use $\sin \Lambda\, |\partial H/\partial \boldsymbol{n}|$ as fringe generator. The fringe pattern convection calculated from the temperature field obtained in the numerical simulations is in very good agreement with the observed experimental data. We conclude here that we are able to validate the experimentally observed images from the 'GeoFlow I' experiment (sheet-like thermal flow) with the numerical model of an ideal isoviscous TEHD driven analogous Rayleigh–Bénard Boussinesq convection system as presented in § 3.

6. Plume-like upwellings in a self-gravitating spherical shell experiment with enhanced viscosity ratio and at higher Rayleigh numbers

6.1. *Experimental observation*

In the following we discuss the observed fringe patterns of convection in the 'GeoFlow II' parameter domain. The experiment itself is performed in two different set-ups. First, the reference cooling circuit is fixed to the lower temperature regime of $T_{ref,min} = 20\,^{\circ}\mathrm{C}$.

Therewith, the initial viscosity of the fluid is higher. Second, the situation is reversed, with the upper limit of $T_{ref,max} = 30\,^{\circ}\mathrm{C}$ and a lower initial viscosity of the fluid. In this case, higher Rayleigh numbers are reached. Figure 3 shows the set points for the Rayleigh number as a function of the viscosity ratio. This ratio results from the properties of the used liquids and remains below 2 for both experiment series. In this illustration with only one Rayleigh number $Ra_{E,cold}/32$ related to the viscosity ratio the possible enhancement by a factor of 32 is not visible. The observation will have to support the illustration in figure 2.

In 'GeoFlow II' an increment of $\Delta T = 0.1$ K delivers $Ra_{E,incr,ref_{min}}/32 = 8.62 \times 10^2$ and $Ra_{E,incr,ref_{max}}/32 = 31.15 \times 10^3$, resulting in a dense scan of the possible domain. For 'GeoFlow I' a flow visualization is only available at the marked symbols, but the whole domain is assessed also via numerical simulation. In addition, in 'GeoFlow I' the cooling circuit is not controlled actively, i.e. it is assumed to be the general room temperature of the ISS. Again, from the illustration in figure 2, it becomes more clear that the two experiment series assess different domains; only the upper 'GeoFlow I' and lower 'GeoFlow II' data can superimpose.

Regarding now the hydrodynamic stability related to figure 1, we do not expect to track the transition from the conductive to the convective flow state above a critical temperature difference and Rayleigh number, respectively. This is visible for the experimental data already at the lowest assessed set points. In general, in the lower Ra domain every single image shows pairs of elliptically formed rings, which are distributed irregularly in the space between the polar and equatorial parts of the spherical research cavity. This fringe pattern of convection clearly corresponds to the plume-like upwelling type. Again, as in the 'GeoFlow I' case, figure 7 combines multiple images. Those spots of plume-like upwelling are depicted in figure 7 for a sample at (*d*) $Ra_{E,cold}/32 = 6.14 \times 10^3$ and (*c*) $Ra_{E,cold}/32 = 1.28 \times 10^4$. Furthermore, patterns are not constant in space and time, changing between measured frames. This is also observed for the mid range of the parameter domain. However, the amount of those time-dependent 'hot spots' increases with viscosity. This has also been observed in numerical models of mantle convection (Hüttig & Breuer 2011).

The overall temporal behaviour of the fluid flow is observed at all stages of the performed set points. Only the specific planforms experience a transition of merged patterns. The plumes are no longer separated from each other but are connected via additional fringes $Ra_{E,cold}/32 = 2.55 \times 10^4$ (figure 7*b*) and $Ra_{E,cold}/32 = 3.81 \times 10^4$ (figure 7*a*). No significant difference in flow patterns is observed between the two different viscosity domains. One might discuss the sharper contrast of the plumes in the higher viscous working environment depicted in the right column of figure 7. From the viewpoint of flow visualization, it is a question of refractive index behaviour. The refractive index is a function of the relative permittivity and the relative permeability. In the case of higher viscosity (higher Pr) the permittivity is also higher. Subsequently the general refractive index level might be higher and lead to more deflection, resulting in more contrast in the images. But there is also another possibility to relate this with a Prandtl number effect. In the real experiment, the two liquids differ in their reference Prandtl number. Starting from 'GeoFlow I' we can calculate $Pr_{ref} = 65$, and in 'GeoFlow II' we get $Pr_{ref,WE\,II} = 200$ and $Pr_{ref,WE\,III} = 125$. At this stage one might identify an influence of the Prandtl number, with higher values inducing sharper contrasts in plume-like upwellings. Clear evidence and an explanation for this influence requires further study, e.g. with further experiments increasing the Prandtl number. In this work here, we will refer to numerical simulations varying the Prandtl number for different models below.

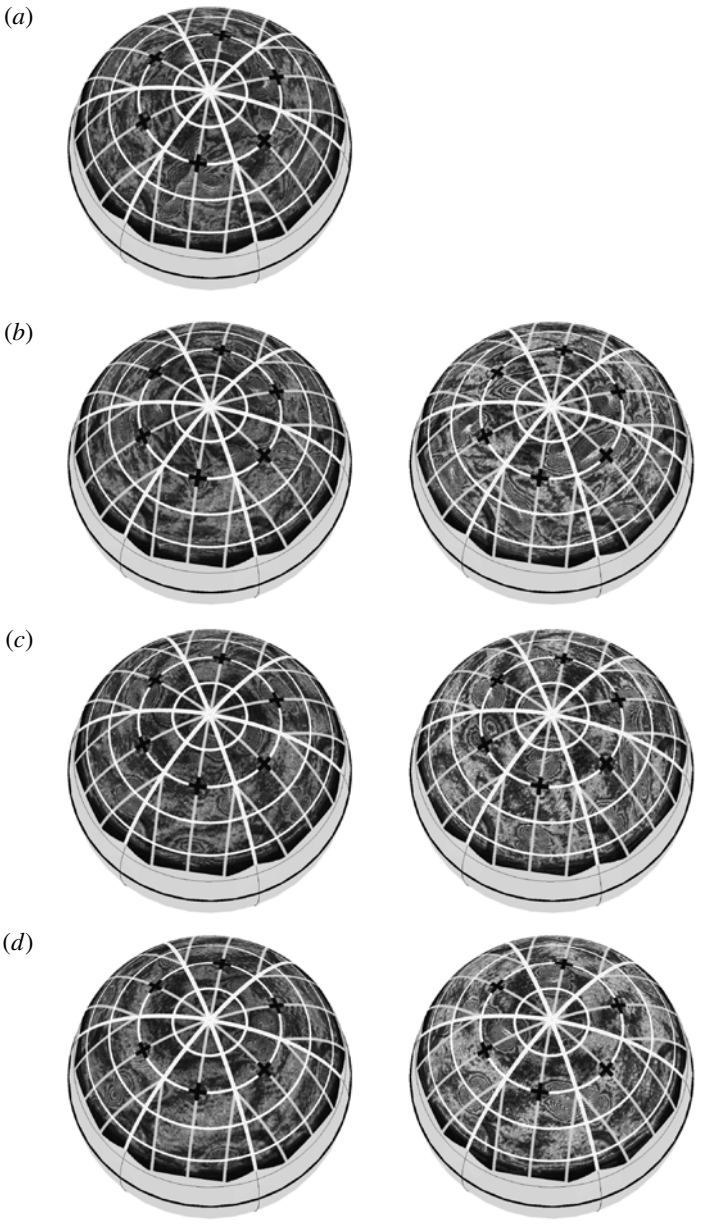

FIGURE 7. The TEHD spherical shell convection experiment 'GeoFlow II' with temperature-dependent physical properties of the liquid (liquid alkanol with $Pr_{T_{ref}=30°C} = 125$ and $Pr_{T_{ref}=20°C} = 200$) and pronounced variation of the viscosity contrast γ in two reference working environments, WE III ($T_{ref} = 30\,°C$), left column, and WE II ($T_{ref} = 20\,°C$), right column. Fringe patterns of convection for variation of the Rayleigh number $Ra_{E,cold}/32$ at different levels of γ: (*a*) 3.81×10^4 (left), (*b*) 2.55×10^4 (left) and 2.56×10^4 (right), (*c*) 1.28×10^4 and 1.28×10^4, and (*d*) 6.14×10^3 and 6.24×10^3. The upper right panel remains empty, because in that lower viscosity regime of WE II this high Rayleigh number is not reached. Parameters below the onset of convection are not observed. The thermal drive produces a plume-like convective planform; the increase of it delivers merged patterns with 'connections' between the plumes. All patterns are snapshots of highly irregular flow.

If we summarize now the route for the parameter domain of both experiment series as depicted in figure 2, we observe sheet-like thermal flow in the lower domain. Then we capture plume-like flow with single sharp spots, connected with broad-banded flow in the upper domain. Especially the plumes are known in simple mantle dynamics with significant viscosity ratios in the stagnant-lid domain. If we observe a plume in our experiment, we can state here that the depth-dependent gravity enhances the viscosity ratio in (3.15). The next step is to validate this result with numerical simulation.

6.2. *Numerical simulation*

In an initial step, we only consider the thermoviscous related terms of our numerical TEHD model in the range of γ below 2 within the non-parallelized spectral code (Hollerbach 2000). Certainly, the TEHD model involves the general factorial difference of 32 between the cold and hot Rayleigh numbers. This does not lead to a change in flow behaviour relative to the constant-viscosity scenario. The spatio-temporal properties of the convective patterns remain comparable to the 'GeoFlow I' cases, i.e. sheet-like. However, the 'GeoFlow II' experimental data show a convection structure dominated by plume-like upwellings, which may be achieved by increasing the effective viscosity ratio. Therefore we use the code GAIA, which can handle high viscosity contrasts (six orders of magnitude between neighbouring grid points and up to 40 system-wide). With GAIA we were already able to validate the results from 'GeoFlow I' with a focus on the influence of the Prandtl number. For the 'GeoFlow II' case, we can increase the parameters even above the effective γ of 32. We also balance the influence of the boundary conditions (no-slip versus free-slip) and the different buoyancy magnitudes (constant, linear and $1/r^5$).

In mantle convection models, free-slip boundary conditions are considered realistic for simulations of the interior dynamics of planetary bodies. However, in a closed experiment, the boundary conditions are automatically set to no-slip. When comparing, for example, the magnitude of velocity between the free-slip and no-slip boundaries for a simulation with a cold Rayleigh number $Ra_{cold} = 6.25 \times 10^2$ and a viscosity contrast $\gamma = 32$, we obtain a velocity that is enhanced by a factor of 2.4 in the free-slip case relative to the no-slip case. This difference is caused by the zero velocity at the boundaries in the no-slip case, while in the free-slip run the lateral velocity can develop freely. This influences the temperature field, resulting in a lower mean temperature for the free-slip case, since heat is transported more efficiently than in the no-slip model. Additionally, the upper thermal boundary layer is located closer to the surface in the free-slip case, meaning that thermal upwellings rise to a shallower depth compared to the no-slip run. All these differences hinder the direct quantitative comparison between the 'GeoFlow' experiments and published mantle convection models.

Therefore, using no-slip boundary conditions in GAIA, we have performed a series of numerical simulations (filled diamonds in figure 2) whose snapshots are shown in figure 8. The critical Rayleigh number was found to be $Ra_{cold,cr} \in (2.1 \times 10^3, 2.2 \times 10^3]$ for an isoviscous mantle system with constant gravity. With a viscosity contrast $\gamma = 32$ we obtain $Ra_{cold,cr} \in (475, 500]$. Performing a numerical simulation for 'GeoFlow' requires a radial dependence. This calculation with GAIA results in a critical onset of $Ra_{E,cold,cr}/32 \in (343.75, 375]$ for 'GeoFlow I'. By increasing either the Rayleigh number or the viscosity contrast, the convection changes from subcritical to steady state and then to time dependent. A time-dependent behaviour is obtained for the simulations plotted above the black border in figure 8. All the simulations in figure 8 are done using a random initial perturbation as appropriate for the comparison

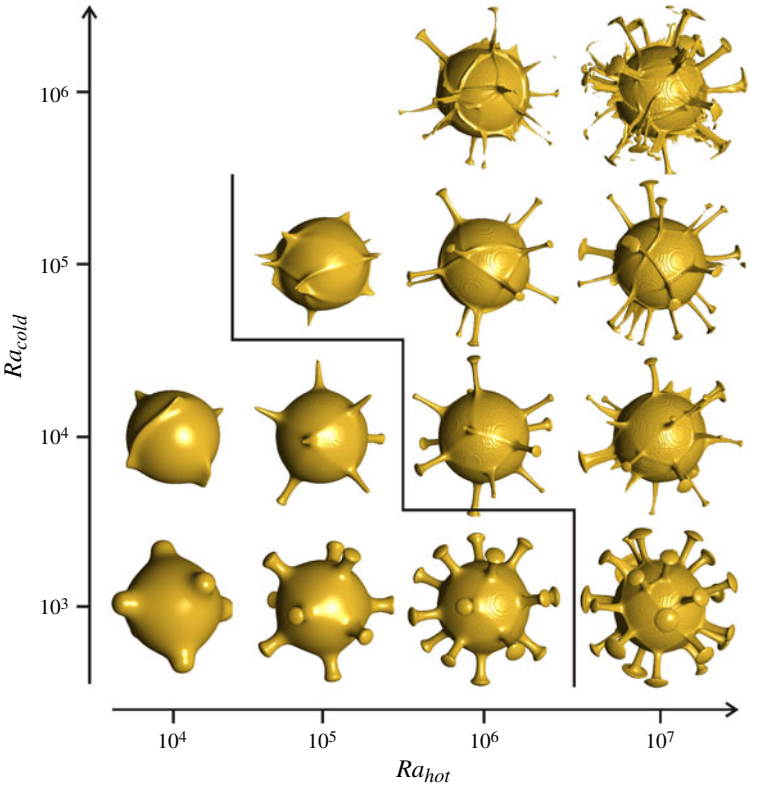

FIGURE 8. (Colour online) Numerical simulation of the mantle Boussinesq model with variation of the viscosity contrast γ: samples at $Ra_{cold} = 10^3,\ 10^4,\ 10^5,\ 10^6$ for $\gamma = 1, \ldots, 10^3$ resulting in $Ra_{hot} = 10^4, \ldots, 10^7$. Patterns of convection are illustrated via an arbitrarily chosen non-dimensional isosurface of the temperature field. The increase of γ leads to plumes, which have a narrower channel of thermal upflow in their stem, when a higher parameter domain and thus a higher thermal driving via Ra_{cold} is considered. Additionally, there are small ridges of thermal upwellings from the hot boundary layer. A time-dependent behaviour is obtained for the simulations plotted above the black border. Refer also to figure 2 for the transition from steady state to unsteady flow regimes.

with the experimental data. Obviously the picture changes if the initial perturbation is set to cubical, for example. The cubical initial conditions result in six upwellings on the axes, which remain stable also for higher Rayleigh numbers (e.g. $Ra_{cold} = 1 \times 10^4$ and $Ra_{hot} = 1 \times 10^6$).

In figure 8 we observe the increase of the number of thermal upwellings with increasing viscosity contrast. This behaviour was also observed in purely internally heated systems with insulating bottom boundary as discussed in Hüttig & Breuer (2011). A low-degree regime as described in Hüttig & Breuer (2011) and Ratcliff *et al.* (1997) has not been found in our simulations. This is most likely to be due to the no-slip boundary conditions, which would prevent a long-wavelength solution (Tackley 1993). It shows once more the importance of the boundary treatment. Additionally, with increasing viscosity ratio, we clearly observe plumes. These plumes have a narrower channel of thermal upflow and a broader head with increasing γ. On increasing the Rayleigh number, the plumes become interconnected by thin sheet-like upwellings along the hot boundary layer.

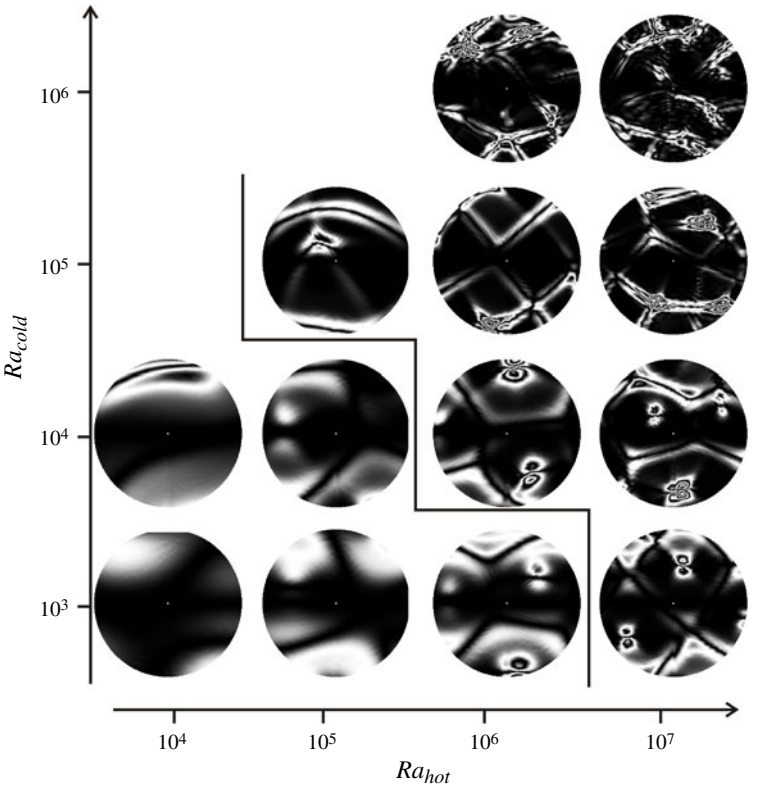

FIGURE 9. Fringe patterns of convection for numerical simulation of the mantle Boussinesq model with variation of the viscosity contrast γ: samples at $Ra_{cold} = 10^3,\ 10^4,\ 10^5,\ 10^6$ for $\gamma = 1, \ldots, 10^3$ resulting in $Ra_{hot} = 10^4, \ldots, 10^7$. Plumes from the lower Ra domain result in clear plume-like fringes with a pair of rings; plumes from the higher Ra domain are not clearly separated as a pair of rings but even merge with sheet-like patterns resulting from the ridges produced in the thermal boundary layer.

Using the flow visualization techniques presented in § 3 we can compute the fringe patterns for the convection structure shown in figure 8. Figure 9 shows the elliptically formed pair of rings representing a plume-like and the continuous lines that indicate a sheet-like upwelling in the upper domain. The stationary regime does not clearly deliver either plume-like flow or sheet-like fringe patterns of convection. At this stage of analysis this is related to the way a temperature profile moves into the optical segment. In the numerical reconstruction of the fringe patterns we are able to vary the position of the optical axis. By this means, we can meet the real situation in the experiment, where the optical axis is fixed and the pattern is moving freely. Figure 10 shows a match of the experimental data with fringe patterns. Here we conclude that the 'GeoFlow II' domain reflects fluid flow dynamics from geodynamic models. The TEHD model seems to be valid only for the higher domain. In the lower regime, only the mantle model is able to validate the observed patterns.

If we briefly summarize that we observe sheets in 'GeoFlow I' and plumes in 'GeoFlow II', one might ask whether there is an influence of the Prandtl number as described in Schmalzl, Breuer & Hansen (2002) and Breuer *et al.* (2004). For very low $Pr \in (0.1, 10)$ they capture a rather low-degree convection pattern with

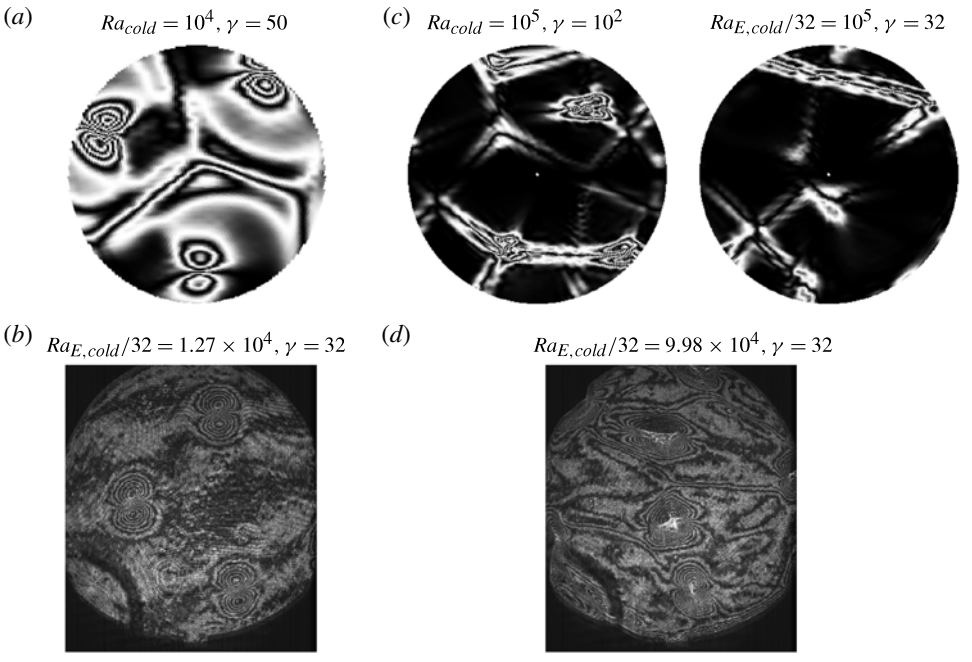

FIGURE 10. Fringe patterns of convection with plume-like thermal upwelling from numerical simulation (top) and observed in a raw image in the experiments (bottom). The lower domain of the experiment exhibits plume-like thermal upwelling; the higher domain is superimposed by sheet-like patterns related to ridges of thermal upwelling in the boundary layer. While the lower domain is only reproduced by a pure mantle model, the higher domain is assessable via both the mantle as well as the TEHD model.

bulgy structures interconnected by sheets in Cartesian box models. In the 'GeoFlow' experiments the Pr numbers used are 64.64, 125 and 200. A first benchmark for 'GeoFlow I', when using an infinite Pr and $Pr = 64.64$ as in the experiment, has shown that in this range the Prandtl number can be assumed to be infinite. In the 'GeoFow II' experiment, Pr is about two times larger than in 'GeoFlow I' and the same argument should hold.

7. Heat transfer properties of convective patterns

In table 5 we show output quantities of the numerical simulations performed in this work. For steady-state simulations three different initial spherical harmonic perturbations of the temperature field have been used: cubic (promotes six upwellings on the axes), tetrahedral (promotes four upwellings distributed in the form of a tetrahedron) or random. Beside the root mean square velocity, average temperature and Nusselt number, we show also the weighted and dominant degree of the convective pattern (Hüttig & Breuer 2011). The latter two offer additional information about the structural complexity being directly correlated with the number of up- and downwellings. In general, for sheet-like thermal structures (for all cases using the 'GeoFlow' configuration) we find that the heat transfer is more effective than for plume-dominated flow as indicated by both higher Nusselt numbers and higher root mean square velocities (table 5). In order to better understand the difference in the convective structure and the cooling behaviour, we select two simulations, where

Case	Ra_{hot}	Set-up	IC	State	v_{rms}	T_{avg}	Nu	W_{mode}	$Mode_{max}$
				$Ra_{cold} = 1 \times 10^3$					
1	1×10^4	Mantle	Cubic	s	5.224	0.287	1.44	4.068	4
2	1×10^4	Mantle	Tetra	s	4.925	0.290	1.41	4.492	4
3	1×10^4	Mantle	Random	s	5.228	0.287	1.43	4.079	4
4	3.2×10^4	Mantle	Random	s	9.825	0.299	1.93	4.690	5
5	3.2×10^4	GeoFlow	Random	s	12.162	0.309	2.19	4.821	4
6	5×10^4	Mantle	Cubic	s	11.813	0.300	2.04	4.091	4
7	5×10^4	Mantle	Tetra	s	11.241	0.296	1.90	3.233	3
8	5×10^4	Mantle	Random	s	11.655	0.304	2.09	5.077	5
9	5×10^4	GeoFlow	Random	s	14.183	0.318	2.35	4.300	4
10	1×10^5	Mantle	Cubic	s	15.938	0.313	2.30	4.154	4
11	1×10^5	Mantle	Tetra	s	15.389	0.309	2.16	3.267	3
12	1×10^5	Mantle	Random	s	15.694	0.321	2.39	5.420	5
13	1×10^5	GeoFlow	Random	s	18.145	0.335	2.62	4.061	4
14	5×10^5	Mantle	Cubic	s	31.408	0.358	2.92	4.493	4
15	5×10^5	Mantle	Tetra	s	29.988	0.374	3.14	6.653	6
16	5×10^5	Mantle	Random	s	29.837	0.371	3.13	6.801	6
17	5×10^5	GeoFlow	Random	s	31.268	0.389	3.17	3.617	3
18	1×10^6	Mantle	Cubic	s	41.779	0.380	3.19	4.712	4
19	1×10^6	Mantle	Tetra	s	39.854	0.394	3.47	6.840	6
20	1×10^6	Mantle	Random	s	38.425	0.394	3.48	7.629	7
21	1×10^6	GeoFlow	Random	s	40.782	0.422	3.51	4.274	3
22	5×10^6	Mantle	Cubic	s	78.619	0.433	3.81	5.287	4
23	5×10^6	Mantle	Tetra	s	71.327	0.442	4.28	8.293	8
24	5×10^6	Mantle	Random	s	71.442	0.442	4.31	8.403	8
25	5×10^6	GeoFlow	Random	s	79.378	0.513	4.53	7.397	6
26	1×10^7	Mantle	Random	t	94.201	0.473	4.78	9.129	8
27	1×10^7	GeoFlow	Random	t	106.808	0.542	4.95	8.524	6
				$Ra_{cold} = 1 \times 10^4$					
28	1×10^4	Mantle	Cubic	s	17.614	0.237	2.33	4.306	4
29	1×10^4	Mantle	Tetra	s	17.525	0.246	2.33	4.137	4
30	1×10^4	Mantle	Random	s	17.521	0.246	2.33	4.146	4
31	5×10^4	Mantle	Cubic	s	27.998	0.256	2.94	4.653	4
32	5×10^4	Mantle	Tetra	s	27.878	0.258	2.96	4.949	4
33	5×10^4	Mantle	Random	s	27.961	0.257	2.97	4.998	4
34	1×10^5	Mantle	Cubic	s	34.123	0.269	3.22	4.848	4
35	1×10^5	Mantle	Tetra	s	33.496	0.273	3.08	3.851	3
36	1×10^5	Mantle	Random	s	34.061	0.272	3.32	5.534	5
37	3.2×10^5	Mantle	Random	s	47.386	0.302	3.97	6.440	5

TABLE 5. (Continued on next page)

Case	Ra_{hot}	Set-up	IC	State	v_{rms}	T_{avg}	Nu	W_{mode}	$Mode_{max}$
38	3.2×10^5	GeoFlow	Random	t	54.575	0.346	3.89	4.441	3
39	5×10^5	Mantle	Cubic	s	54.335	0.307	3.94	5.384	4
40	5×10^5	Mantle	Tetra	s	54.163	0.312	4.22	6.701	5
41	5×10^5	Mantle	Random	s	53.272	0.318	4.33	7.389	6
42	5×10^5	GeoFlow	Random	t	62.396	0.371	4.20	4.659	3
43	1×10^6	Mantle	Cubic	s	66.611	0.326	4.27	5.622	4
44	1×10^6	Mantle	Tetra	s	66.095	0.332	4.72	7.567	6
45	1×10^6	Mantle	Random	s	65.412	0.339	4.69	7.400	6
46	1×10^6	GeoFlow	Random	t	75.160	0.402	4.73	6.306	3
47	5×10^6	Mantle	Random	t	105.899	0.401	5.79	8.763	8
48	5×10^6	GeoFlow	Random	t	127.284	0.491	6.06	8.519	6
49	1×10^7	Mantle	Random	t	132.916	0.426	6.17	8.519	7
50	1×10^7	GeoFlow	Random	t	169.208	0.526	6.93	9.240	7
				$Ra_{cold} = 1\times10^5$					
51	1×10^5	Mantle	Random	t	71.098	0.230	3.92	5.86	3
52	5×10^5	Mantle	Random	t	102.466	0.267	5.25	7.16	5
53	1×10^6	Mantle	Random	t	122.292	0.285	5.96	7.234	5
54	3.2×10^6	Mantle	Random	t	165.579	0.327	7.20	8.411	7
55	3.2×10^6	GeoFlow	Random	t	203.597	0.409	7.43	9.230	6
56	5×10^6	Mantle	Random	t	193.870	0.348	7.74	8.455	7
57	5×10^6	GeoFlow	Random	t	229.889	0.424	8.07	9.602	6
58	1×10^7	Mantle	Random	t	229.528	0.367	8.55	8.975	6
59	1×10^7	GeoFlow	Random	t	297.573	0.454	9.10	9.357	5
				$Ra_{cold} = 1\times10^6$					
60	1×10^6	Mantle	Random	t	270.387	0.227	7.74	8.742	6
61	5×10^6	Mantle	Random	t	379.040	0.284	10.32	9.111	6
62	1×10^7	Mantle	Random	t	446.289	0.307	11.47	8.834	8

TABLE 5. Results for the cases presented in this work: Ra_{hot} and Ra_{cold} are the Rayleigh numbers at the inner and outer boundary. The set-up shows either the use of a pure mantle model or the 'GeoFlow' TEHD model. Initial starting conditions (IC) vary between cubic, tetrahedral or random. In the fourth column of the table we show whether the simulations reached a steady-state (s) or a time-dependent state (t). Further quantities are the root mean square velocity v_{rms}, average temperature T_{avg} and Nusselt number Nu, respectively. The output parameters W_{mode} and $Mode_{max}$ give information about the spherical harmonics degrees. While W_{mode} is a weighted spherical harmonics degree, $Mode_{max}$ is the dominant degree reached.

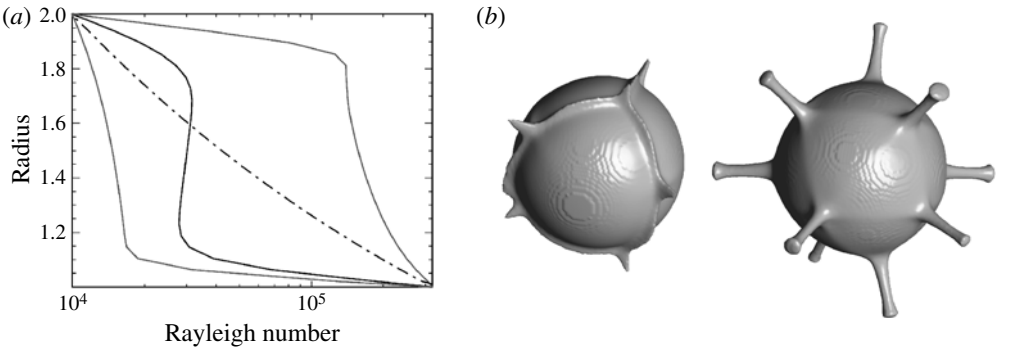

FIGURE 11. Influence of the self-gravitating configuration on the variation of the buoyancy term and the convective patterns. (*a*) Variation of the buoyancy term caused by either a temperature-dependent viscosity (grey lower full line, maximum; grey upper full line, minimum; black line, volume averaged) or $1/r^5$ as used in the 'GeoFlow' experiments (dashed-dotted line). (*b*) Convection patterns obtained for $Ra_{cold} = 10^4$ and $Ra_{hot} = 3.2 \times 10^5$ (the buoyancy term increases towards the inner boundary): left, the buoyancy term changes with $1/r^5$; right, the buoyancy term changes due to the temperature-dependent viscosity.

the Rayleigh number varies either (i) locally due to temperature-dependent viscosity (viscosity decreases with increasing temperature) according to $\mu(T) = \exp(-\gamma T)$ with $\gamma = \ln(32)$ or (ii) as $1/r^5$ ('GeoFlow' configuration and with constant viscosity). The Rayleigh numbers at the inner and outer boundary in these simulations are the same ($Ra_{cold} = 10^4$ and $Ra_{hot} = 3.2 \times 10^5$) but vary with depth as in figure 11(*a*). The volume-averaged Rayleigh number is 3.43×10^4 for the temperature-dependent viscosity case and 6.24×10^4 for the 'GeoFlow' configuration. Thus, the increase of the Nusselt number for the sheet-like thermal structures are related to a higher effective Rayleigh number.

In the case of the 'GeoFlow' configuration, the lower thermal boundary layer is therefore more unstable than in the case where the Rayleigh number changes solely due the temperature-dependent viscosity. The first scenario shows sheet-like structures while the latter produces a plume-like flow (figure 11*b*). However, on increasing the Rayleigh number at the outer boundary above 10^4, both the sheet-like and the plume-like structures change to a structure that shows plumes interconnected by sheets. This structure is independent of the depth dependence of the Rayleigh number. An interconnection between individual plumes has also been observed by Houseman (1990) in three-dimensional Cartesian box models with stress-free boundaries and was associated with convection patterns at high Rayleigh numbers in at least partially bottom-heated systems.

8. Summary, discussion and outlook

In this paper we present results from our 'GeoFlow' spherical convection experiments performed under microgravity, which use an analogy of TEHD convection to reflect a Rayleigh–Bénard system in a spherical experiment. In the first experiment 'GeoFlow I' we use a silicone oil (M5), whose physical properties are considered to be temperature-independent. In the second experiment 'GeoFlow II' we keep the experimental design and set-up and fill the research cavity with an alkanol (1-nonanol), whose properties are comparable to the silicone oil except for a pronounced

variability of the viscosity with temperature. This allows us to capture the initial basis of hydrodynamic effects in a spherical experiment motivated by Earth's mantle convection phenomena. The experimental domain captures several orders of the thermal driving parameter, i.e. the Rayleigh number, along with an enhanced viscosity ratio of 32. To the best of our knowledge this has been treated by means of numerical simulations only (figure 1) or in rather complex experiments in rectangular geometries (Androvandi *et al.* 2011). After a discussion of the governing equations and specific properties of the TEHD convection, we present the results from both experiment series and benchmark them against numerical simulation. We observe a sheet-like thermal flow (visible in our flow visualization as interferograms of fringes), when the physical properties of the fluid do not vary with temperature – a result from 'GeoFlow I'. When we use a liquid with temperature-dependent viscosity ('GeoFlow II'), we observe a plume-like dominated flow (visible in the interferograms as pairs of concentrically organized ellipsoidal rings). For the 'GeoFlow I' situation we are able to reproduce our sheet-like fringe patterns of convection. Both available numerical codes, Hollerbach (2000) and GAIA, describe the equations of the system with just a TEHD related buoyancy term. Hence, we prove experimentally that the symmetry classes for patterns of convection in a spherical shell system are more or less generic. Only the details depend on the specific functional form of the gravitational potential. Using the example of a cubic symmetry, a mantle model with constant gravity delivers plume patterns of convection, called cubic, if four plumes are upwelling from the equator (Bercovici *et al.* 1989*a*). A cubic symmetry formed by four upwellings connected with sheets in the upper and lower hemisphere is discussed in Busse (1975) and Busse & Riahi (1982) for a linear dependence of the gravitational potential. Here, we describe it for a $1/r^5$ dependence resulting from the TEHD model. All patterns in the 'GeoFlow I' domain are independent of the Prandtl number ($Pr > 50$). Thus the experiment can be considered as a Stokes flow.

For the 'GeoFlow II' case the situation is rather different, as we depict in figure 10. Dividing the plume-like fringe patterns of convection into two mainly observed types, the single plumes in the lower domain and the superimposed ridges in the higher domain, we are able to reproduce them with some additional conditions. For the single plumes, which are not interconnected by sheet-like upwellings, we have an agreement with a mantle model, i.e. without $1/r^5$ dependence of the buoyancy term. For the higher domain both the mantle as well as the TEHD model deliver the same result. In both cases we see evidence that depth-dependent gravity acts via an enhancement of the viscosity contrast. Thus, if using a pure TEHD model, γ is directly comparable. However, if instead a mantle model is used, then γ needs to be higher. Figure 12 shows how the patterns obtained with the numerical simulations correlate to the structures obtained in the 'GeoFlow' experiments and demonstrates the inconsistency between the numerical and the 'GeoFlow II' experiment for low surface Rayleigh number. It still remains to be clarified why for the temperature-dependent viscosity ('GeoFlow II') the convection pattern changes from sheet-like to plume-like. To this end more experimental data (expected from a subsequent 'GeoFlow IIb' mission) and numerical simulations are needed.

When we compare the combination of experimental and numerical work for the TEHD issues, we have the results from Hart *et al.* (1986), where a very good agreement between experimental and numerical data is found. But the authors use a temperature equation different from ours. They include on the right side of our equation (3.11) a term related to the dissipative heating and, in addition, they add a

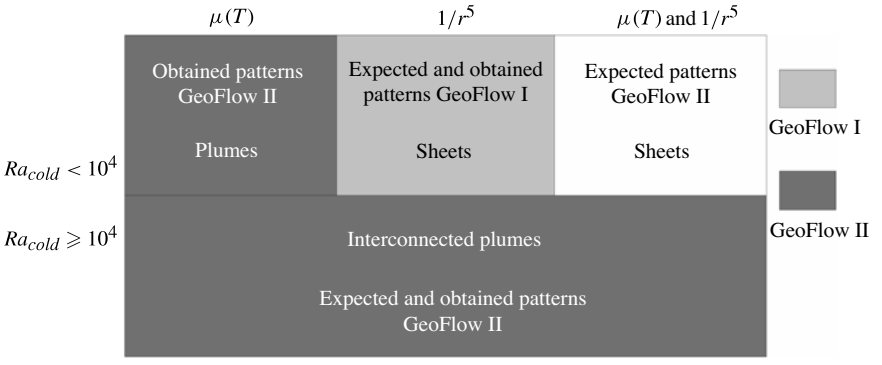

FIGURE 12. Parameter space and corresponding structures obtained in the numerical study. The pattern domains obtained in the two GeoFlow experiments are shown in different grey shades.

term 'depending on $\boldsymbol{E}$ that represents the work done by electric forces' (Hart *et al.* 1986, p. 522):

$$\frac{\partial \varepsilon}{\partial t} T \frac{\mathrm{D}E^2}{\mathrm{D}t} / 2\rho c. \tag{8.1}$$

In our pre-studies for 'GeoFlow I' we omitted this term as a result of an extended discussion related to its effective contribution to the flow (Travnikov *et al.* 2003). Our 'GeoFlow I' results support this approach. Considering the TEHD in the vertical annulus as in Malik *et al.* (2012) and Yoshikawa *et al.* (2013), we have a comparable discussion on the so-called feedback effect, i.e. via the Gauss equation $\nabla \cdot (\varepsilon \boldsymbol{E}) = 0$, taking into account the influence 'on the temperature disturbances on the electric permittivity' (Malik *et al.* 2012). Thus they keep the same temperature equation as in our model. While an extended numerical study would deliver an answer as to which of the other two TEHD equation models fit our experimental observation, we might assume that in the lower domain we have such feedback effects producing the single plumes not reflected in our recent TEHD model.

It has to be mentioned again that we have an agreement also in our selected tests in the Earth laboratory. But in the microgravity the permittivity replaces the density. For 1-nonanol, the liquid of 'GeoFlow II', the feedback effect seems to play a more important role than for M5, the liquid of 'GeoFlow I'. Owing to technical pre-studies, we act on the assumption that our used liquids do not suffer from fatigue. Nevertheless, we summarize that we are able to reproduce plume-like flow in a spherical experiment by means of TEHD experiments.

In December 2012 we started the mission 'GeoFlow IIb', which will support more highly resolved analysis related to the time resolution of the flow modes. In addition, the transient behaviour will be reviewed. Both require long-term observations, which were only authorized after the second mission 'GeoFlow II', which lasted from March 2011 until May 2012. To clarify the feedback effects we plan to perform additional parameter sets on orbit with a variation of the high-voltage potential. This will distinguish the temperature effects on the permittivity as we vary the electric energy.

Acknowledgements

The 'GeoFlow' project is funded by ESA (grant no. AO-99-049) and by the German Aerospace Center DLR (grant nos. 50 WM 0122 and 50 WM 0822). The authors would also like to thank ESA for funding the 'GeoFlow' Topical Team (grant no. 18950/05/NL/VJ). The scientists also thank the industrial companies involved for their support, namely Astrium GmbH, Friedrichshafen, Germany, the User Support and Operations Center, MARS Telespazio, Naples, Italy and E-USOC, Madrid, Spain.

During the main part of this work, the first author (B.F.) was supported by the Brandenburg Ministry of Science, Research and Culture (MWFK) as part of the International Graduate School at Brandenburg University of Technology (BTU). From 1 October 2012, B.F. holds a one-year visiting professorship at the Otto von Guericke Universität, Magdeburg, funded through the Saxony-Anhalt Ministry of Economics and Research (MWW). R.H. is supported at ETH Zürich by the European Research Council (grant no. 247303 (MFECE)).

Furthermore, fruitful discussions with Anne Davaille, Laboratoire FAST, CNRS/UPMC Université Paris Sud, Orsay, France, and Olivier Crumeyrolle, Harunori Yoshikawa and Innocent Mutabazi, Laboratoire Ondes et Milieux Complexes, UMR 6294, CNRS Université du Havre, France, are gratefully acknowledged.

We thank the Northern German Network for High-Performance Computing (HLRN) for the computer resources used for the parallelized calculations.

REFERENCES

ANDROVANDI, S., DAVAILLE, A., LIMAREA, A., FOUCQUIERA, A. & MARAIS, C. 2011 At least three scales of convection in a mantle with strongly temperature-dependent viscosity. *Phys. Earth Planet. Inter.* **188**, 132–141.

BAHLOUL, A., MUTABAZI, I. & AMBARI, A. 2000 Codimension 2 points in the flow inside a cylindrical annulus with a radial temperature gradient. *Eur. Phys. J., Appl. Phys.* **9**, 253–264.

BAUMGARDNER, J. P. 1985 Three-dimensional treatment of convective flow in the Earth's mantle. *J. Stat. Phys.* **39**, 501–511.

BAYER LEVERKUSEN (now GE Bayer Silicones Germany). 2002 Bayer Silicones: Baysilone Fluids M. Technical Data Sheet, 11.11.2002 (delivered with the liquids).

BERCOVICI, D., SCHUBERT, G. & GLATZMAIER, G. A. 1989*a* Three-dimensional spherical models of convection in the Earth's mantle. *Science* **244**, 950–955.

BERCOVICI, D., SCHUBERT, G. & GLATZMAIER, G. A. 1991 Modal growth and coupling in three-dimensional spherical convection. *Geophys. Astrophys. Fluid Dyn.* **61**, 149–159.

BERCOVICI, D., SCHUBERT, G. & GLATZMAIER, G. A. 1992 Three-dimensional convection of an infinite-Prandtl-number compressible fluid in a basally heated spherical shell. *J. Fluid Mech.* **239**, 683–719.

BERCOVICI, D., SCHUBERT, G., GLATZMAIER, G. A. & ZEBIB, A. 1989*b* Three-dimensional thermal convection in a spherical shell. *J. Fluid Mech.* **206**, 75–104.

BOOKER, J. R. 1976 Thermal convection with strongly temperature-dependent viscosity. *J. Fluid Mech.* **76**, 741–754.

BREUER, M., WESSLING, S., SCHMALZL, J. & HANSEN, U. 2004 Effects of inertia in Rayleigh–Bénard convection. *Phys. Rev.* E **69**, 026302.

BUSSE, F. H. 1975 Patterns of convection in spherical shells. *J. Fluid Mech.* **72**, 67–85.

BUSSE, F. H. 1978 Non-linear properties of thermal convection. *Rep. Prog. Phys.* **41**, 1930–1967.

BUSSE, F. H. 2002 Convective flows in rapidly rotating spheres and their dynamo action. *Phys. Fluids* **14**, 1301–1313.

BUSSE, F. H. & FRICK, H. 1985 Square-pattern convection in fluids with strongly temperature-dependent viscosity. *J. Fluid Mech.* **150**, 451–465.

BUSSE, F. H. & RIAHI, N. 1982 Patterns of convection in spherical shells. Part 2. *J. Fluid Mech.* **182**, 283–301.

CHANDRASEKHAR, S. 1981 *Hydrodynamic and Hydromagnetic Stability*. Dover.

CHRISTENSEN, U. & HARDER, H. 1991 Three-dimensional convection with variable viscosity. *Geophys. J. Intl* **104**, 213–226.

CULLEN, M. 2007 Modelling atmospheric flows. *Acta Numerica* **16**, 67–154.

DAVAILLE, A. & JAUPART, C. 1994 Onset of thermal convection in fluids with temperature-dependent viscosity: application to the oceanic mantle. *J. Geophys. Res.* **99**, 19 843–19 866.

DAVAILLE, A. & LIMARE, A. 2009 Laboratory studies of mantle convection. In *Mantle Dynamics* (ed. G. Schubert & D. Bercovici), Treatise on Geophysics, 7, pp. 89–165. Elsevier.

DUBOIS, F., JOHANNES, L., DUPONT, O., DEWANDEL, J. L. & LEGROS, J. C. 1999 An integrated optical set-up for fluid physics experiments under microgravity conditions. *Meas. Sci. Technol.* **10**, 934–945.

DUTTON, J. A. 1995 *Dynamics of Atmospheric Motion*. Dover.

EGBERS, C., BEYER, W., BONHAGE, A., HOLLERBACH, R. & BELTRAME, P. 2003 The GEOFLOW-experiment on ISS (Part I): Experimental preparation and design. *Adv. Space Res.* **32**, 171–180.

FEUDEL, F., BERGEMANN, K., TUCKERMAN, L., EGBERS, C., FUTTERER, B., GELLERT, M. & HOLLERBACH, R. 2011 Convection patterns in a spherical fluid shell. *Phys. Rev.* E **83**, 046304.

FIZ CHEMIE (Fachinformationszentrum Chemie GmbH, Berlin). 2010 Relative permittivity at zero frequency. 2010-03-29, ID 1972shkgal0, http://www.fiz-chemie.de/infotherm/.

FUTTERER, B., BRUCKS, A., HOLLERBACH, R. & EGBERS, C. 2007 Thermal blob convection in spherical shells. *Intl J. Heat Mass Transfer* **50**, 4079–4088.

FUTTERER, B., DAHLEY, N., KOCH, S., SCURTU, N. & EGBERS, C. 2012 From isoviscous convective experiment 'GeoFlow I' to temperature-dependent viscosity in 'GeoFlow II' – Fluid physics experiments on-board ISS for the capture of convection phenomena in Earth's outer core and mantle. *Acta Astronaut.* **71**, 11–19.

FUTTERER, B., EGBERS, C., DAHLEY, N., KOCH, S. & JEHRING, L. 2010 First identification of sub- and supercritical convection patterns from GeoFlow, the geophysical flow simulation experiment integrated in Fluid Science Laboratory. *Acta Astronaut.* **66**, 193–200.

FUTTERER, B., SCURTU, N., EGBERS, C., PLESA, A.-C. & BREUER, D. 2009 Benchmark on Prandtl number influence for GeoFlow II, a mantle convection experiment in spherical shells. In *Proceedings of the 11th International Workshop on Modelling of Mantle Convection and Lithospheric Dynamics, Braunwald, Switzerland.*

HANSEN, U. & YUEN, D. A. 1993 High Rayleigh number regime of temperature-dependent viscosity convection and the Earth's nearly thermal history. *Geophys. Res. Lett.* **20**, 2191–2194.

HANSEN, U. & YUEN, D. A. 1994 Effects of depth-dependent thermal expansivity on the interaction of thermal chemical plumes with a compositional boundary. *Phys. Earth Planet. Inter.* **86**, 205–221.

HART, J. E., GLATZMAIER, G. A. & TOOMRE, J. 1986 Space-Laboratory and numerical simulations of thermal convection in a rotating hemispherical shell with radial gravity. *J. Fluid Mech.* **173**, 519–544.

HÉBERT, F., HUFSCHMID, R., SCHEEL, J. & AHLERS, G. 2010 Onset of Rayleigh–Bénard convection in cylindrical containers. *Phys. Rev.* E **81**, 046318.

HERNLUND, J. W. & TACKLEY, P. J. 2008 Modelling mantle convection in the spherical annulus. *Earth Planet. Sci. Lett.* **274**, 380–391.

HOLLERBACH, R. 2000 A spectral solution of the magneto-convection equations in spherical geometry. *Intl J. Numer. Meth. Fluids* **32**, 773–797.

HOUSEMAN, G. A. 1990 The thermal structure of mantle plumes: axisymmetric or triple junction?. *Geophys. J. Intl* **102**, 15–24.

HÜTTIG, C. & BREUER, D. 2011 Regime classification and planform scaling for internally heated mantle convection. *Phys. Earth Planet. Inter.* **186**, 111–124.

HÜTTIG, C. & STEMMER, K. 2008*a* Finite volume discretization for dynamic viscosities on Voronoi grids. *Phys. Earth Planet. Inter.* **171**, 137–146.

HÜTTIG, C. & STEMMER, K. 2008*b* The spiral grid: a new approach to discretize the sphere and its application to mantle convection. *Geochem. Geophys. Geosyst.* **9**, Q02018.

JONES, T. B. 1979 Electrohydrodynamically enhanced heat transfer in liquids – a review. *Adv. Heat Transfer* **14**, 107–148.

KAMEYAMA, M. & OGAWA, M. 2000 Transitions in thermal convection with strongly temperature-dependent viscosity in a wide box. *Earth Planet. Sci. Lett.* **180**, 355–367.

KELLOGG, L. H. & KING, S. D. 1997 The effect of temperature dependent viscosity on the structure of new plumes in the mantle: results of a finite element model in a spherical, axisymmetric shell. *Earth Planet. Sci. Lett.* **148**, 13–26.

LANDAU, L. D., LIFSHITZ, E. M. & PITAEVSKII, L. D. 1984 *Course of Theoretical Physics – Electrodynamics of Continuous Media*. Butterworth-Heinemann.

LIDE, D. R. 2008 *Handbook of Chemistry and Physics*. CRC Press.

MALIK, S. V., YOSHIKAWA, H. N., CRUMEYROLLE, O. & MUTABAZI, I. 2012 Thermo-electro-hydrodynamic instabilities in a dielectric liquid under microgravity. *Acta Astronaut.* **81**, 563–569.

MAZZONI, S. 2011 GeoFlow II experiment scientific requirements. RQ 3. European Space Agency ESA, European Space Research and Technology Centre ESTEC, Noordwijk, The Netherlands, reference SCI-ESA-HSF-ESR-GEOFLOW II.

MERCK (Merck KGaA Darmstadt, Germany). 2003 1-Nonanol zur Synthese. Safety Data Sheet 806866, 28.05.2003 (delivered with the liquids).

MERZKIRCH, W. 1987 *Flow Visualization*. Academic Press.

MORRIS, S. & CANRIGHT, D. R. 1984 A boundary-layer analysis of Bénard convection with strongly temperature-dependent viscosity. *Earth Planet. Sci. Lett.* **36**, 355–377.

NATAF, H. C. & RICHTER, F. M. 1982 Convection experiments in fluids with highly temperature-dependent viscosity and the thermal evolution of the planets. *Phys. Earth Planet. Inter.* **29**, 320–329.

OGAWA, M. 2008 Mantle convection: a review. *Fluid Dyn. Res.* **40**, 379–398.

OGAWA, M., SCHUBERT, G. & ZEBIB, A. 1991 Numerical simulations of three-dimensioanl thermal convection a fluid with strongly temperature-dependent viscosity. *J. Fluid Mech.* **233**, 299–328.

RATCLIFF, J. T., SCHUBERT, G. & ZEBIB, A. 1996 Effects of temperature-dependent viscosity on thermal convection in a spherical shell. *Physica* D **97**, 242–252.

RATCLIFF, J. T., TACKLEY, P. J., SCHUBERT, G. & ZEBIB, A. 1997 Transitions in thermal convection with strongly variable viscosity. *Phys. Earth Planet. Inter.* **102**, 201–212.

RICHTER, F. M., NATAF, H. C. & DALY, S. F. 1983 Heat transfer and horizontally averaged temperature of convection with large viscosity variations. *J. Fluid Mech.* **129**, 173–192.

SCHMALZL, J., BREUER, M. & HANSEN, U. 2002 The influence of the Prandtl number on the style of vigorous thermal convection. *Geophys. Astrophys. Fluid Dyn.* **96**, 381–403.

SCHUBERT, G. & BERCOVICI, D. 2009 *Mantle Dynamics*, 7, Treatise on Geophysics, Elsevier.

SCHUBERT, G., GLATZMAIER, G. A. & TRAVIS, B. 1993 Steady, three-dimensional, internally heated convection. *Phys. Fluids* A **5**, 1928–1932.

SCHUBERT, G. & OLSON, P. 2009 *Treatise on Geophysics – Core Dynamics*. Elsevier.

SCURTU, N., FUTTERER, B. & EGBERS, C. 2010 Pulsating and travelling wave modes of natural convection in spherical shells. *Phys. Fluids* **22**, 114108.

SOLOMATOV, V. S. 1995 Scaling of temperature and stress-dependent viscosity convection. *Phys. Fluids* **7**, 266–274.

STEMMER, K., HARDER, H. & HANSEN, U. 2006 A new method to simulate convection with strongly temperature- and pressure-dependent vicosity in a spherical shell: applications to the Earth's mantle. *Phys. Earth Planet. Inter.* **157**, 223–249.

STENGEL, K. C., OLIVER, D. S. & BOOKER, J. R. 1982 Onset of convection in a variable-viscosity fluid. *J. Fluid Mech.* **120**, 411–431.

SUGIYAMA, K., CALZAVARINI, E., GROSSMANN, S. & LOHSE, D. 2007 Non-Oberbeck–Boussinesq effects in two-dimensional Rayleigh–Bénard convection in glycerol. *Europhys. Lett.* **80**, 34002.

TACKLEY, P. J. 1993 Effects of strongly temperature-dependent viscosity on time-dependent three-dimensional models of mantle convection. *Geophys. Res. Lett.* **20**, 2187–2190.

TACKLEY, P. J. 1996 Effects of strongly variable viscosity on three-dimensional compressible convection in planetary mantles. *J. Geophys. Res.* **101**, 3311–3332.

TRAVNIKOV, V., EGBERS, C. & HOLLERBACH, R. 2003 The GEOFLOW-experiment on ISS (Part II): numerical simulation. *Adv. Space Res.* **32**, 181–189.

WHITE, D. B. 1988 The planforms and onset of convection with a temperature-dependent viscosity. *J. Fluid Mech.* **191**, 247–286.

YANAGISAWA, T. & YAMAGISHI, Y. 2005 Rayleigh–Bénard convection in spherical shell with infinite Prandtl number at high Rayleigh number. *J. Earth Sim.* **4**, 11–17.

YAVORSKAYA, I. M., FOMINA, N. I. & BALYAEV, Y. N. 1984 A simulation of central symmetry convection in microgravity conditions. *Acta Astronaut.* **11**, 179–183.

YOSHIKAWA, H. N., CRUMEYROLLE, O. & MUTABAZI, I. 2013 Dielectrophoretic force-driven thermal convection in annular geometry. *Phys. Fluids* **25**, 024106.

ZHANG, J., CHILDRESS, S. & LIBCHABER, A. 1997 Non-Boussinesq effect: thermal convection with broken symmetry. *Phys. Fluids* **9**, 1034–1042.

ZHANG, P., LIAO, X. & ZHANG, K. 2002 Patterns in spherical Rayleigh–Bénard convection: a giant spiral roll and its dislocations. *Phys. Rev. E* **66**, 055203.

ZHONG, S., MCNAMARA, A., TAN, E., MORESI, L. & GURNIS, M. 2008 A benchmark study on mantle convection in a 3-D spherical shell using CitcomS. *Geochem. Geophys. Geosyst.* **9**, Q10017.

ZHONG, S., ZUBER, M. T., MORESI, L. & GURNIS, M. 2000 Role of temperature-dependent viscosity and surface plates in spherical shell models of mantle convection. *J. Geophys. Res.* **105** (B5), 11 063–11 082.